Lithos 316–317 (2018) 122–136

Contents lists available at ScienceDirect

Lithos

journal homepage: www.elsevier.com/locate/lithos

Petrogenesis of basalts along the eastern Woodlark spreading center, equatorial western Pacific

Sung-Hyun Park [a,*], Peter J. Michael [b], George D. Kamenov [c], Sang-Mook Lee [d], Folkmar Hauff [e], Kyeong Yong Lee [f]

[a] Korea Polar Research Institute, Incheon, South Korea
[b] Department of Geosciences, The University of Tulsa, 800 S. Tucker Drive, Tulsa, OK 74104, USA
[c] Department of Geological Sciences, University of Florida, Gainesville FL32611, USA
[d] School of Earth and Environmental Sciences, Seoul National University, Seoul, South Korea
[e] GEOMAR Helmholtz Centre for Ocean Research Kiel, Germany
[f] Deep-Sea Resources Research Program, Korea Institute of Ocean Science and Technology, Ansan, P.O. Box 29, Seoul, Republic of Korea

ARTICLE INFO

Article history:
Received 16 November 2017
Accepted 2 July 2018
Available online 6 July 2018

Keywords:
Woodlark Basin
Basalts
Sub-arc residual mantle
Residual eclogite

ABSTRACT

Seafloor spreading in the Woodlark Basin is taking place on pre-existing arc crust that was produced by the subduction of the Indo-Australian Plate into the Pocklington Trough (now inactive) to the south during the Paleogene. The Woodlark Basin has a unique tectonic setting characterized by two surrounding subduction zones. To the east, a spreading ridge is also currently being subducted beneath the Solomon Arc. Moreover, long-term subduction of the Pacific Plate occurred in this area, which was halted by the collision of the Ontong–Java Plateau with the Vitiaz Trench at ca. 10 Ma. Any one of these subduction zones could have influenced the mantle beneath the Woodlark Basin. In this study, basalts from the eastern Woodlark Basin spreading center (EWLB; eastern Woodlark Basin basalts) were analyzed for major and trace element compositions and Sr-Nd-Pb isotopic compositions to investigate the melting processes and mantle heterogeneity in this unusual tectonic setting. Our results show that the EWLB can be classified into three types based on major and trace elements, and Sr–Nd–Pb isotopic characteristics: normal EWLB (N-EWLB), very depleted EWLB (VD-EWLB), and ultra-depleted EWLB (UD-EWLB). N-EWLB are similar to normal mid-ocean ridge basalts (N-MORB) and comprise most of the EWLB. The EWLB formed from local mantle, which is similar to depleted MORB mantle. VD-EWLB are more depleted than N-EWLB and have a weak subduction fingerprint. These rocks are characterized by increasing Nb/La with increasing Sm/La, which is a trend that is not produced by peridotite melting. As such, VD-EWLB may have formed by melting of a source containing residual eclogite that had previously undergone low-degree partial melting during subduction, leaving residual rutile in the source. UD-EWLB are extremely depleted relative to global MORB, have elevated H_2O/Ce and Ba/Nb ratios similar to back-arc basin basalts (BABB), and lower concentrations of H_2O and Ba than N-MORB. We propose that UD-EWLB was derived from sub-arc residual mantle that was enriched by fluid and then experienced melt depletion. The subduction fingerprints in the VD- and UD-EWLB are not related to the current ridge subduction or earlier, long-term subduction of the Pacific Plate in the northeast of the basin, as they are geochemically distinct from the Solomon Arc, which was strongly influenced by both these subduction systems. Instead, we suggest that the subduction fingerprint of the VD- and UD-EWLB was produced during Paleogene subduction of the Indo-Australian Plate to the south.

© 2018 Elsevier B.V. All rights reserved.

1. Introduction

Normal mid-ocean ridge basalts (N-MORB) are derived from mantle sources that are depleted in incompatible elements such as Ba, Nb, and La relative to the primitive mantle (e.g., Salters and Stracke, 2004; Workman and Hart, 2005). The limited range in the degree of depletion observed in N-MORB today is thought to be due to homogenization by subsequent mantle convection (e.g., Faure, 1986 and references therein), but some basalts derived from other tectonic settings are much more depleted than N-MORB. For example, arc and back-arc basalts are highly depleted in high-field-strength elements (HFSE) relative to N-MORB (Pearce et al., 2005; Pearce and Peate, 1995; Pearce and Stern, 2006; Sinton and Fryer, 1987). Ultra-depleted basalts are also found along some mid-ocean ridges, particularly at transform faults and off-axis seamounts (Michael and Graham, 2015). These highly depleted rocks might be related to local tectonic processes, but the

* Corresponding author at: Korea Polar Research Institute, 26 Songdomirae-ro, Incheon 21990, Republic of Korea.
E-mail address: shpark314@kopri.re.kr (S.-H. Park).

https://doi.org/10.1016/j.lithos.2018.07.003
0024-4937/© 2018 Elsevier B.V. All rights reserved.

petrogenesis of highly depleted basalts in various tectonic settings has not been studied in great detail.

In 2000, we dredged the eastern spreading segments of the Woodlark Basin to investigate melting processes and mantle heterogeneity in this tectonic setting. Amongst the dredged samples, we found basalts that were much more depleted than global N-MORB. In this paper, we investigate how these highly depleted rocks were generated in this tectonic setting.

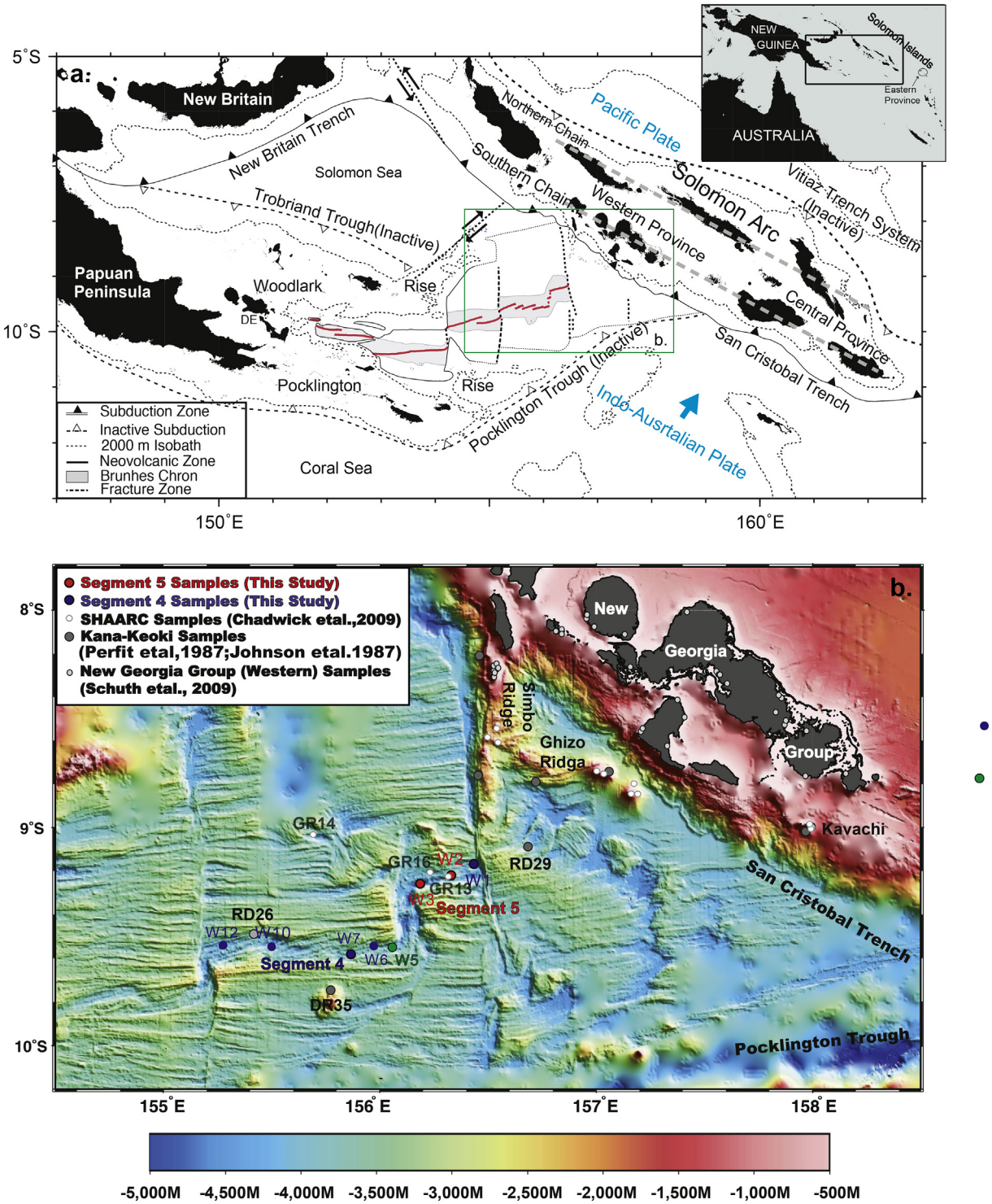

Fig. 1. Tectonic and bathymetric maps. a) Tectonic map of the Woodlark Basin (modified from Goodliffe et al., 1997). Inset shows the locations of the Woodlark Basin and Solomon Arc (including the eastern Solomon Arc). Red lines show the axis of the Woodlark Spreading Center. Gray dashed lines indicate the northern and southern chains of the Solomon Arc (Schuth et al., 2009). b) Bathymetric map showing the dredge locations along the eastern Woodlark Spreading Center (bathymetric data were provided by A. Goodliffe). Red numbers and circles on the neovolcanic zone indicate dredge numbers from Segment 5, whereas blue and green numbers and circles are from Segment 4. Other sampling locations in the Solomon Arc, Kavachi volcano, and Ghizo and Simbo ridges are also plotted as gray or white circles, as are the samples from Chadwick et al. (2009).

2. Tectonic history and setting of the Woodlark Basin

The Woodlark Basin is a 500-km-long marginal basin located to the east of Papua New Guinea and south of the Solomon Islands. It has been described as a back-arc basin (e.g., Kelley et al., 2006), but it should be considered a local basin with a spreading center in the middle, because there is no active subduction zone or arc parallel to its spreading center (Fig. 1). The Woodlark spreading center (WSC) started opening at ca. 5 Ma on the remnant arc crust ("New Guinea Arc") that was produced by the northeastward subduction of the Indo-Australian Plate from 45 to 25 Ma into the Pocklington Trough, southwest of the present-day Woodlark Basin (Karig, 1972; Pigram and Symonds, 1991; Schellart et al., 2006; Taylor, 1987; Worthing and Crawford, 1996). Currently, the WSC is continuing to propagate westward, and has separated the New Guinea Arc into the Woodlark and Pocklington rises (Fig. 1a) since it started opening at 5 Ma. The WSC has five clearly defined segments, from Segment 1 in the west to Segment 5 in the east, and these may have been synchronously reoriented since 80 ka (Fig. 1a; Goodliffe et al., 1997).

Long-term southwestward subduction of the Pacific Plate took place along the North Solomon Trench (Vitiaz Trench in the present system; Fig. 1) to the northeast of the Woodlark Basin from the Cretaceous until 10 Ma. The collision of the Ontong–Java Plateau caused the cessation of Pacific Plate subduction along the North Solomon Trench and the initiation of a new subduction zone along the New Britain and San Cristobal trenches at 10 Ma. This resulted in a reversal of subduction polarity (Cooper and Taylor, 1985; Schellart et al., 2006). The easternmost Woodlark Basin, including the spreading center, is part of the Indo-Australian Plate and is currently being subducted eastward into the San Cristobal Trench beneath the New Georgia Group (Fig. 1b; Taylor and Exon, 1987; Schellart et al., 2006). This forms part of the Solomon Arc. The Ghizo Ridge is located at the easternmost end of the Woodlark Basin and is thought to be a fossil spreading center that is undergoing subduction (Perfit et al., 1987; Taylor, 1987). The Simbo Ridge may be a leaky transform connecting Segment 5 and the Ghizo Ridge (Perfit et al., 1987). The subduction of the WSC is one of two examples of the subduction of an active spreading center worldwide; the other case is the Chile Ridge–Trench triple junction (Klein and Karsten, 1995).

The 1000-km-long Solomon Arc consists of two volcanic chains that lie between the inactive Vitiaz Trench to the north and the active San Cristobal Trench to the south (Fig. 1). The northern chain formed during subduction of the Pacific Plate, whereas the southern chain was produced mainly by the subduction of the Indo-Australian Plate (Schuth et al., 2009). The southern chain of the Solomon Arc was divided by Schuth et al. (2009) into the western, central, and eastern provinces (Fig. 1). The New Georgia Group, beneath which the eastern Woodlark Basin is now subducting, is part of the western province in the southern chain of the Solomon Arc (Fig. 1b). Kavachi is the most active volcano in the New Georgia Group.

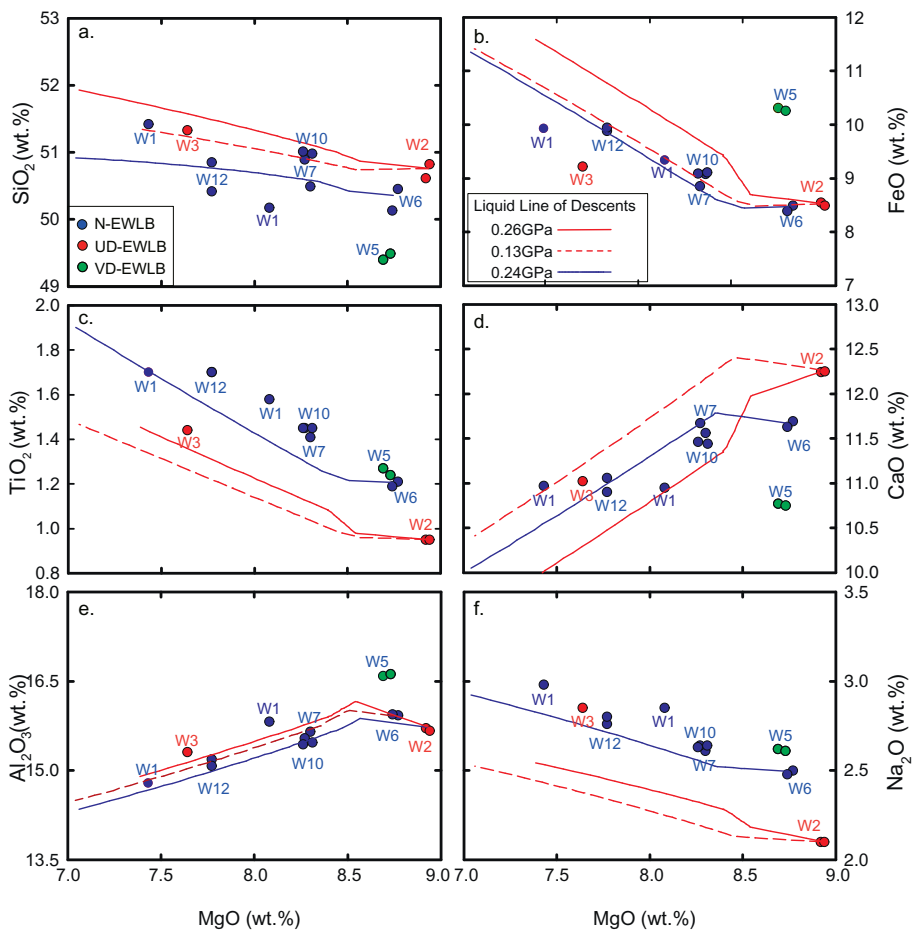

Fig. 2. Major element variations of eastern Woodlark Basin glasses. Model trends were derived using Petrolog 3.1.1 (Danyushevsky and Plechov, 2011). Pressures were chosen to best match the observed data. The pressures are shown in the legend and were assumed to be constant for each run. dT/dP of saturation for olivine, plagioclase, and clinopyroxene were 4°/kbar, 4°/kbar, and 8°/kbar, respectively. The crystal–melt models of Danyushevsky (2001) and default H_2O dependencies were used in running Petrolog 3.1.1. Model lines terminate on the left side at 40% crystallization. H_2O contents input to the modeling were adjusted to slightly lower values in all cases to better fit the data. Model lines match the general trends of the data. The poor fit for some elements, especially Na and Ti of UD-EWLB, demonstrates that the primary magmas are variable along the spreading axes, but some of this deviation may also result from variable crystallization histories.

Table 1
Major (wt%), trace (ppm) elements concentrations and isotope ratios of eastern Woodlark Basalt (glasses).

Sample	Segment 5					Segment 4											ARV 2392 (T)*	ARV 2392 (L)*	Stdev (L)*
	W1–3	W1–4	W2–1	W2–2	W3–2	W5–1	W5–2	W6–1	W6–2	W7–1	W7–2	W7–2 _rep.	W10–1	W10–2	W12–1	W12–2			
SiO_2	51.42	50.17	50.61	50.82	51.33	49.40	49.49	50.45	50.13	50.49	50.89		51.01	50.98	50.85	50.42			
TiO_2	1.70	1.58	0.95	0.95	1.44	1.27	1.24	1.21	1.19	1.41	1.45		1.45	1.45	1.70	1.70			
Al_2O_3	14.79	15.82	15.71	15.67	15.31	16.59	16.62	15.93	15.94	15.65	15.54		15.44	15.47	15.19	15.08			
FeO	9.93	9.34	8.55	8.49	9.22	10.31	10.26	8.49	8.39	9.08	8.85		9.09	9.11	9.88	9.94			
MnO	0.20	0.15	0.13	0.13	0.18	0.22	0.22	0.18	0.20	0.22	0.12		0.16	0.16	0.19	0.22			
MgO	7.43	8.08	8.92	8.94	7.64	8.69	8.73	8.77	8.74	8.30	8.27		8.26	8.31	7.77	7.77			
CaO	10.97	10.95	12.24	12.25	11.02	10.77	10.75	11.69	11.63	11.56	11.67		11.46	11.44	11.06	10.90			
Na_2O	2.98	2.85	2.10	2.10	2.85	2.62	2.61	2.50	2.48	2.61	2.64		2.63	2.64	2.76	2.80			
K_2O	0.07	0.07	0.03	0.04	0.06	0.04	0.044	0.06	0.06	0.08	0.06		0.07	0.07	0.097	0.101			
P_2O_5	0.12	0.12	0.07	0.07	0.13	0.10	0.09	0.08	0.06	0.15	0.15		0.15	0.15	0.14	0.16			
H_2O	0.223	0.212	0.118	0.118	0.371	0.171	0.168	0.156	0.151	0.202	0.208		0.193	0.197	0.288	0.291			
Total	99.8	99.3	99.4	99.6	99.6	100	100	99.5	99.0	99.7	99.8		99.9	100.0	99.9	99.4			
Cl		0.0017	0.0044		0.0062	0.0009	0.0014	0.0024	0.0009	0.0004	0.0009		0.0012	0.0010	0.0034	0.0042			
F		0.0112	0.0053		0.0152	0.0133	0.0149	0.0073	0.0065	0.0155	0.0249		0.0143	0.0115	0.0205	0.0171			
S		0.1182	0.1121		0.1182	0.1200	0.1205	0.1094	0.1081	0.1177	0.1232		0.1180	0.1187	0.1244	0.1281			
Mg#	59.71	63.14	67.40	67.59	62.14	62.52	62.76	67.17	67.35	64.42	64.92		64.28	64.37	60.90	60.75			
Li		5.92	4.58	4.83	6.20	3.88	3.98	4.86	5.14		5.41		5.63	5.65	6.36	6.29	5.24	5.21	0.23
Sc		32.2	31.4	32.2	32.4	31.0	32.7	31.9	33.3		34.2		34.3	34.2	34.9	34.7	37.6	37.6	0.40
V		261	218	222	243	221	219	219	226		250		251	261	280	288	259	257	4.18
Cr		254	367	379	303	328	308	339	360		375		345	330	259	266	325	322	12.35
Co		37.2	39.1	39.4	38.7	44.6	42.7	36.4	39.0		37.2		41.1	36.7	38.3	38.8	41.0	40	0.83
Ni		117	120	124	132	175	157	127	136		114		160	108	112	119	114	112	1.95
Cu		58.9	80.1	81.5	69.0	79.0	79.4	65.8	68.4		64.0		63.1	63.7	57.6	57.8	73.5	73.3	1.29
Zn		74.9	66.7	66.4	78.0	77.2	75.2	66.8	68.9		71.3		74.6	73.5	79.4	80.9	73.4	73.57	2.01
Ga		16.2	14.2	14.5	16.5	15.4	15.6	14.7	16.0		15.7		15.9	16.2	16.7	17.3	16.3	15.5	0.40
Rb		0.48	0.41	0.41	0.59	0.32	0.34	0.37	0.38		0.44		0.46	0.47	0.72	0.72	0.90	0.87	0.07
Sr		113	58	59	76	95	96	105	109		108		100	103	116	118	119	116	3.5
Y		34.9	23.9	24.0	33.7	27.9	27.3	26.5	27.4		30.5		31.8	32.3	36.3	36.7	28.6	28.6	0.5
Zr		99.8	40.2	40.5	79.1	64.1	64.2	67.5	69.4		80.3		83.9	84.9	102.9	103.3	78.4	79.9	2.2
Nb		1.19	0.33	0.33	0.77	1.44	1.21	0.96	0.99		1.22		1.13	1.15	1.61	1.61	2.10	2.10	0.093
Cs		0.0073	0.0069	0.0065	0.0089	0.0040	0.0041	0.0052	0.0044		0.0064		0.0078	0.0081	0.0194	0.0197	0.0104	0.0127	0.0024
Ba		2.77	3.01	2.93	4.43	1.94	1.76	2.05	2.13		2.59		2.61	2.60	3.83	3.88	7.75	7.5	0.9
La		2.70	1.02	1.02	2.03	1.61	1.58	2.07	2.13		2.53		2.49	2.51	3.20	3.10	2.86	2.84	0.135
Ce		9.45	3.83	3.83	7.58	5.55	5.42	7.09	7.29		8.50		8.56	8.62	10.69	10.37	9.00	8.97	0.392
Nd		9.35	4.71	4.75	8.44	5.96	5.80	7.12	7.30		8.15		8.51	8.55	10.15	9.84	8.24	8.39	0.24
Sm		3.34	1.96	1.97	3.20	2.39	2.33	2.57	2.66		2.94		3.09	3.08	3.59	3.48	2.87	2.88	0.04
Pr		1.70	0.77	0.77	1.46	1.02	1.00	1.27	1.31		1.50		1.53	1.55	1.86	1.82	1.54	1.54	0.082
Eu		1.18	0.79	0.80	1.15	0.95	0.93	0.99	1.00		1.07		1.11	1.12	1.26	1.22	1.05	1.07	0.02
Gd		4.50	2.99	2.97	4.42	3.55	3.43	3.56	3.65		3.99		4.18	4.23	4.81	4.66	3.87	3.85	0.07
Tb		0.85	0.57	0.57	0.83	0.68	0.65	0.67	0.68		0.75		0.78	0.79	0.90	0.87	0.71	0.71	0.01
Dy		5.45	3.79	3.79	5.41	4.47	4.30	4.30	4.42		4.87		5.09	5.12	5.80	5.63	4.63	4.58	0.10
Ho		1.17	0.82	0.82	1.16	0.96	0.94	0.91	0.94		1.04		1.08	1.10	1.25	1.21	0.99	0.99	0.02
Er		3.38	2.38	2.40	3.35	2.81	2.74	2.64	2.70		3.03		3.13	3.18	3.59	3.50	2.84	2.80	0.05
Tm		0.51	0.36	0.37	0.51	0.43	0.42	0.40	0.41		0.46		0.48	0.49	0.55	0.53	0.43	0.43	0.01
Yb		3.38	2.35	2.38	3.31	2.79	2.73	2.58	2.63		2.96		3.06	3.14	3.54	3.49	2.83	2.74	0.06
Lu		0.51	0.36	0.36	0.50	0.43	0.41	0.39	0.40		0.45		0.47	0.48	0.54	0.54	0.42	0.42	0.01
Hf		2.63	1.36	1.33	2.36	1.80	1.76	1.89	1.93		2.20		2.32	2.34	2.79	2.68	2.11	2.13	0.06
Ta		0.09	0.02	0.02	0.06	0.11	0.09	0.07	0.07		0.09		0.08	0.08	0.12	0.12	0.15	0.14	0.01
Pb		0.34	0.17	0.17	0.23	0.21	0.21	0.28	0.29		0.28		0.26	0.26	0.42	0.37	0.28	0.29	0.10
Th		0.072	0.029	0.027	0.054	0.039	0.036	0.048	0.051		0.065		0.061	0.062	0.088	0.086	0.12	0.12	0.01
U		0.034	0.019	0.018	0.028	0.023	0.023	0.029	0.029		0.037		0.033	0.035	0.049	0.046	0.05	0.05	0.00

(continued on next page)

Table 1 (*continued*)

Sample	Segment 5					Segment 4											ARV 2392 (T)*	ARV 2392 (L)*	Stdev (L)*
	W1–3	W1–4	W2–1	W2–2	W3–2	W5–1	W5–2	W6–1	W6–2	W7–1	W7–2	W7–2_rep.	W10–1	W10–2	W12–1	W12–2			
Dy/Yb	**1.61**	**1.61**	**1.61**	**1.60**	**1.63**	**1.60**	**1.58**	**1.67**	**1.68**		**1.65**		**1.66**	**1.63**	**1.64**	**1.61**			
Sr/Nd	**12.1**		**12.3**	**12.5**	**9.0**	**16.0**	**16.6**	**14.7**	**14.9**		**13.3**		**11.7**	**12.1**	**11.4**	**11.9**			
$^{87}Sr/^{86}Sr$			**0.702689**	**0.702692**	**0.702628**	**0.702777**		**0.702556**			**0.702594**	**0.702586**	**0.702567**		**0.702590**				
2 Sigma			0.000003	0.000003	0.000003	0.000003		0.000003			0.000003	0.000006	0.000003		0.000003				
$^{143}Nd/^{144}Nd$			**0.513127**	**0.513130**	**0.513123**	**0.513104**		**0.513115**			**0.513100**	**0.513098**	**0.513102**		**0.513098**				
2 Sigma			0.000003	0.000003	0.000003	0.000002		0.000002			0.000003	0.000003	0.000003		0.000003				
eNd			**9.54**	**9.60**	**9.46**	**9.09**		**9.30**			**9.02**		**9.06**		**8.97**				
$^{206}Pb/^{204}Pb$			**18.1080**	**18.1111**	**18.1259**	**18.1466**		**18.2320**			**18.2363**	**18.2367**	**18.1725**		**18.3001**				
2 Sigma			0.0008	0.0009	0.0017	0.0006		0.0006			0.0009	0.0007	0.0006		0.0007				
$^{207}Pb/^{204}Pb$			**15.4626**	**15.4647**	**15.4682**	**15.4661**		**15.4697**			**15.4740**	**15.4739**	**15.4648**		**15.4828**				
2 Sigma			0.0007	0.0008	0.0015	0.0005		0.0006			0.0010	0.0009	0.0006		0.0007				
$^{208}Pb/^{204}Pb$			**37.7658**	**37.7734**	**37.7801**	**37.7730**		**37.8295**			**37.8495**	**37.8499**	**37.7912**		**37.9097**				
2 Sigma			0.0020	0.0022	0.0045	0.0015		0.0014			0.0032	0.0029	0.0018		0.0019				

*ARV2392: Internal Standard used in Geological Sciences, University of Florida. ARV2392 (T): Run with these samples, *ARV2392 (L): Long Term Analysis, Stdev(L): Standard Deviation for Long Term Analysis.

3. Results

We dredged basalts from eight different sites along Segments 4 and 5 of the eastern WSC (EWSC) during a cruise by the R/V Onnuri (Fig. 1b; Supplementary Table 1). This region was poorly sampled before our survey. A German research cruise to the Woodlark Basin by the RV Sonne in 2009 (Devey, 2009) focused on the western Woodlark Basin and did not obtain samples from the easternmost segments. The dredge samples are fresh porphyritic basalts that contain 7%–8% plagioclase phenocrysts. Glasses were chipped from the outer glass rinds of large samples and analyzed for major, trace, and volatile elements, and Sr–Nd–Pb isotopic compositions using electron microprobe, HR–ICP–MS (High-Resolution Inductively Coupled Plasma Mass-Spectrometry), FT–IR (Fourier-Transform Infrared Spectroscopy), and TIMS (Thermal Ionization Mass Spectrometry) techniques, respectively. [Please consider defining these acronyms, even though these are well-known techniques.] The analytical methods are described in Appendix A.

3.1. Major elements

The glasses contain 7.43–8.94 wt% MgO, but the majority of samples have >8 wt% MgO and are quite primitive (Fig. 2). Silica contents range from 48.6 to 51.5 wt% and alkali contents ($Na_2O + K_2O$) are low and vary from 2.13 to 3.05 wt%. Thus, all samples from the eastern Woodlark Basin are tholeiitic basalts (Fig. 2; Table 1) and are similar to MORB in their major element composition. Plots of major elements versus MgO show trends for several samples that are consistent with low-pressure crystallization (Fig. 2; e.g., Langmuir et al., 1992). For example, Fig. 2e shows that plagioclase joined olivine as a fractionating phase at ~8.5 wt% MgO.

The major element variation diagrams show that samples W1 and W6–W12 were derived from similar parental magmas, but the other samples may have been derived from different parental magmas. For example, W2 is the most primitive glass, but has Na_2O and TiO_2 contents that are too low for it to have been a parental magma for samples W1 and W6–12 (Fig. 2c and f). Sample W3 is more fractionated than W2, but is also low in Na_2O and TiO_2 at a given MgO as compared with samples W1 and W6–12. Similarly, sample W5 is too high in Al_2O_3 and FeO, and low in CaO, at a given MgO content to have been a parental magma for the other samples (Fig. 2b, d, and e.).

3.2. Trace elements and H_2O

Samples W1 and W6–12 are similar to N-MORB in their primitive-mantle-normalized trace element patterns, although they are very slightly enriched in Cs, Rb, and U (Fig. 3). Notably, data for these samples plot amongst the most depleted basalts in the global MORB dataset (Gale et al., 2013; Fig. 4). Based on their trace element characteristics, samples W1 and W6–12 could have been derived by varying degrees of crystallization from similar parental magmas, and are defined here as normal eastern Woodlark Basin basalts (N-EWLB).

Sample W5 is more depleted than N-EWLB, with slight enrichment in Nb and Ta compared with similarly incompatible elements (Figs 3 and 4), such as La. Sample W5 is lower in Ba/Nb and Zr/Y, and higher in Nb/La and Sm/La than N-EWLB (Fig. 4d and f). Sample W5 also has elevated H_2O/Ce ratios compared with N-EWLB and the Lau Basin minimum (a back-arc), but it has lower Ba/Nb ratios than the other samples (Fig. 5). Given that W5 can be distinguished from N-EWLB based on its major and trace element features, we define it as very depleted EWLB (VD-EWLB).

Samples W2 and W3 are more depleted in light rare earth elements (LREE) and HFSE than N-EWLB (Fig. 3a) and VD-EWLB. For example, the La/Sm ratios of W2 and W3 indicate that they are more depleted than other samples (Fig. 4e). These samples are slightly enriched in fluid-mobile elements (e.g., Cs, Rb, and U) relative to Nb, and are similar to some

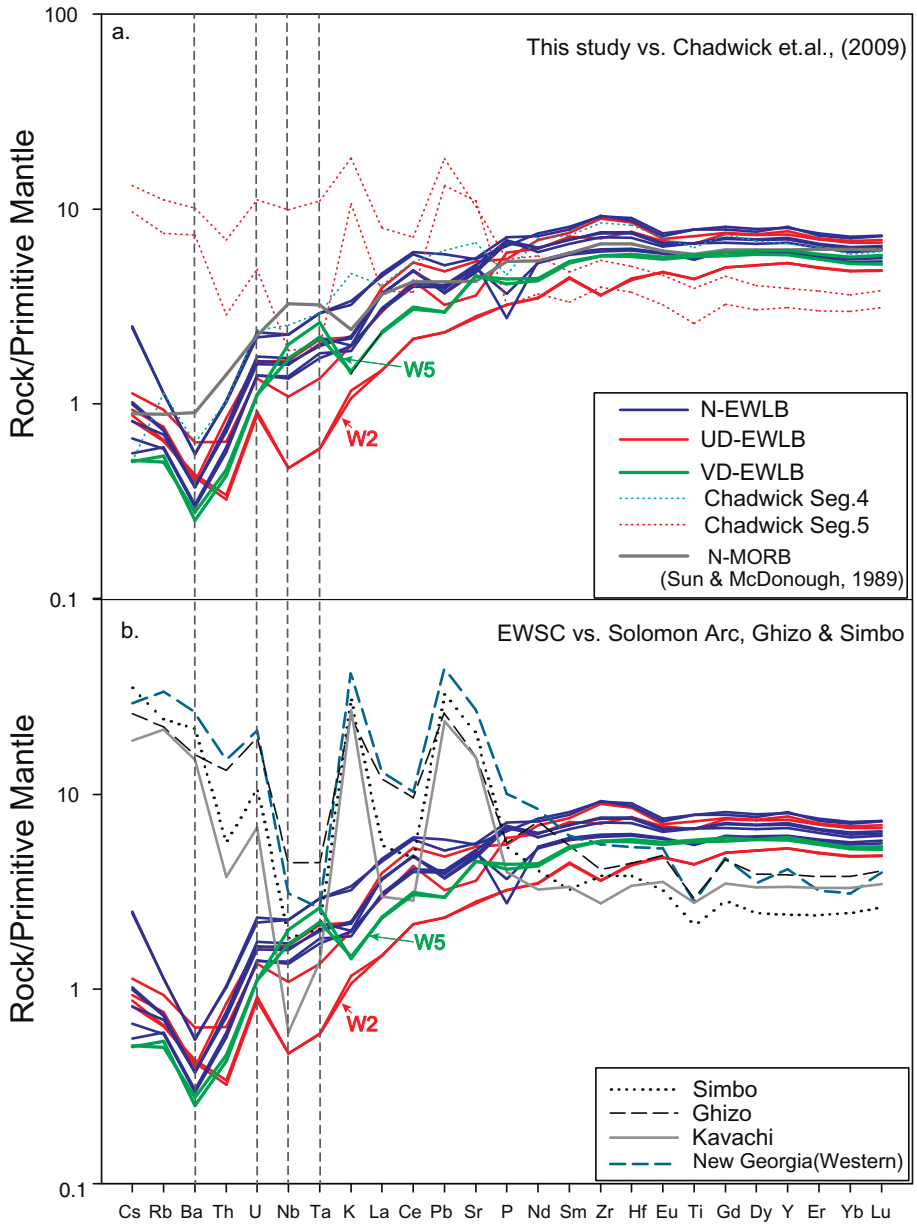

Fig. 3. Trace element spider diagram normalized to primitive mantle (Sun and McDonough, 1989). All EWLB lavas are more depleted than the N-MORB values from Sun and McDonough (1989). a) Comparison of data from this study with those of Chadwick et al. (2009) for Segments 4 and 5. GR13 and GR16 (thin red dashed lines) are from Segment 5, and GR14 (thin blue dashed line) is from off-axis of Segment 4 (Fig. 1a). GR13 and GR16 are different from Segment 5 samples of our study. b) Comparison between the Solomon Arc (New Georgia and Kavachi) and Ghizo and Simbo ridges in the Woodlark Basin. New Georgia, Kavachi, Ghizo, and Simbo data are averaged values. The data for the Solomon Arc are from König and Schuth (2011) and Schuth et al. (2009). The data from Kavachi volcano, and Ghizo and Simbo ridges are from Chadwick et al. (2009).

back-arc basin basalts (BABB) that have a slight subduction fingerprint (Figs 3 and 4; Gill, 1976; Sun and McDonough, 1989; Pearce et al., 2005; Pearce and Stern, 2006). Figures 4 and 5 clearly show that H_2O/Ce and Ba/Nb ratios for samples W2 and W3 (located in the central and western parts of Segment 5, respectively) are greater than the Lau–Mariana minimum (Gale et al., 2013), indicating that subduction components are present in their mantle source. It is important to note that the concentrations of the fluid-mobile elements Ba, Pb, and H_2O in W2 are lower than in N-EWLB (Figs 3a and 5c). Ce/Pb ratios are ~22, and enrichment of Pb relative to Ce is not observed (Fig. 4e). Here, we define these samples as ultra-depleted EWLB (UD-EWLB), as they are extremely depleted compared with the global MORB dataset and have different trace element patterns to those of N-EWLB.

3.3. Sr–Nd–Pb isotopes and incompatible trace element ratios

N-, VD-, and UD-EWLB have different radiogenic isotope ratios to each other. UD-EWLB have higher $^{87}Sr/^{86}Sr$ and $^{143}Nd/^{144}Nd$ ratios than N-EWLB, and VD-EWLB have higher $^{87}Sr/^{86}Sr$ ratios as compared with N-EWLB and UD-EWLB. UD-EWLB have lower $^{206}Pb/^{204}Pb$ ratios and are offset to slightly higher $^{208}Pb/^{204}Pb$ and $^{207}Pb/^{204}Pb$ ratios for a given $^{206}Pb/^{204}Pb$, compared with N-EWLB (Fig. 6c; Table 1).

Differences in radiogenic isotope ratios between the sample types are also correlated with incompatible trace element ratios (Fig. 7). N-and UD-EWLB show positive correlations between $^{87}Sr/^{86}Sr$ and Ba/Nb (Fig. 7a), and VD-EWLB has lower Ba/Nb ratios relative to N-EWLB, but higher $^{87}Sr/^{86}Sr$. VD-EWLB has high Nb/La and $^{87}Sr/^{86}Sr$ ratios. It is notable that $^{143}Nd/^{144}Nd$ ratios are positively correlated with Zr/Y ratios

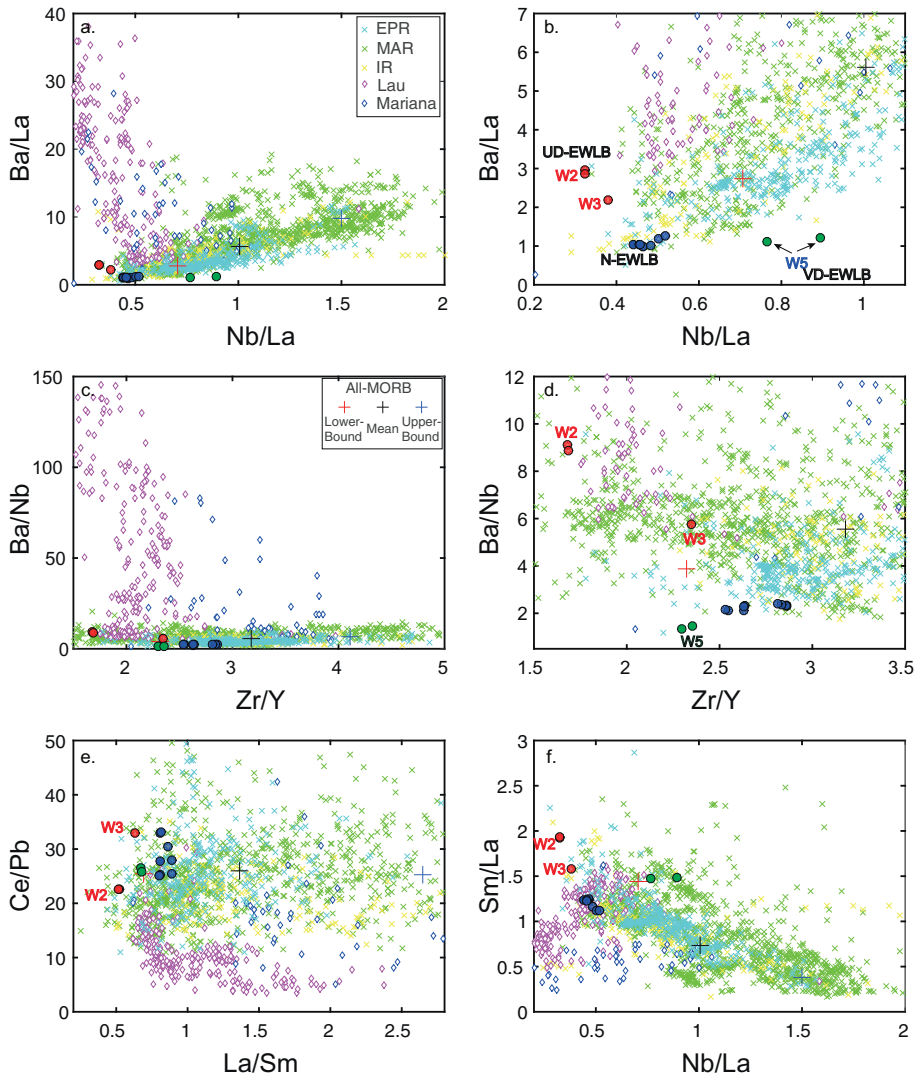

Fig. 4. Incompatible trace element ratio plots compared with global data for MORB and BABB (Gale et al., 2013). All-MORB Mean is the averaged global MORB composition (Gale et al., 2013), excluding BABB. All-MORB lower and upper bounds are 95% confidence limits of the global MORB data (Gale et al., 2013). EWLBs are more depleted than or similar to the All-MORB lower bound. a, b) Ba/La versus Nb/La. Panel a) has a larger scale than panel b). c, d) Ba/Nb versus Zr/Y. Panel c) has a larger scale than panel d). e) Ce/Pb versus La/Sm. La/Sm values of EWLB lavas are near the lower bound of All-MORB, and their Ce/Pb values are similar to the All-MORB mean. Ce/Pb values for BABB from the Lau Basin are <10 where La/Sm is >0.75, but increase steeply to the All-MORB mean where La/Sm = 0.50–0.75. Ce/Pb values of Mariana lavas are scattered and generally higher than those of Lau lavas. f) Sm/La versus Nb/La. The V-shaped trends in panels b) and f) can be explained by the mixing of two different and highly depleted components with the mantle source of N-EWLB lavas. Note that the compositions of Lau and Mariana BABB cross the global MORB array in different directions. Data for EWLB lavas show different trends to those for Lau and Mariana lavas.

for the entire sample suite. However, a plot of $^{206}Pb/^{204}Pb$ versus Ce/Pb shows no correlation.

Lead isotopic systematics of the EWLB indicates derivation from Indian Ocean-type mantle, similar to basalts from other Western Pacific marginal basins (Fig. 6d). Indian-type oceanic crust has different isotopic systematics from Pacific-type oceanic crust. For example, $^{208}Pb/^{204}Pb$ and $^{207}Pb/^{204}Pb$ ratios of Indian-type oceanic crust are slightly more radiogenic at a given $^{206}Pb/^{204}Pb$ than for Pacific-type oceanic crust (Klein et al., 1988).

4. Discussion

EWLB may be classified into three types based on major and trace elements, and radiogenic isotope ratios, as shown above: N-, VD-, and UD-EWLB. Differences between the three sample types cannot be explained by fractional crystallization from similar parental magmas. In this section, we investigate the petrogenesis of each basalt type.

4.1. N-EWLB (samples W1 and W6–W12)

N-EWLB display almost no subduction signature in terms of elevated H_2O and fluid-mobile element (e.g., Ba and Cl) contents (Figs 3 and 4; Table 1), suggesting that they represent the composition of local upper mantle. N-EWLB have very low Nb/La, La/Sm, and Zr/Y ratios relative to global MORB (Gale et al., 2013), suggesting their source is more depleted than the average N-MORB source (Fig. 4). Using a two-stage melting model and Zr/Y and La/Sm data (Fig. 8), we evaluated the extent of source depletion relative to an average N-MORB source and the degree of partial melting to produce N-EWLB.

Using the depleted mantle composition of Salters and Stracke (2004), variably depleted sources were calculated using the fractional melting equation (Shaw, 1970). It is generally accepted that the mantle melts by a fractional melting process rather than by batch melting (Johnson et al., 1990; Langmuir et al., 1992; Pearce and Parkinson, 1993).

Trajectories of second-stage melts from the variably depleted sources were calculated using batch melting equations, because

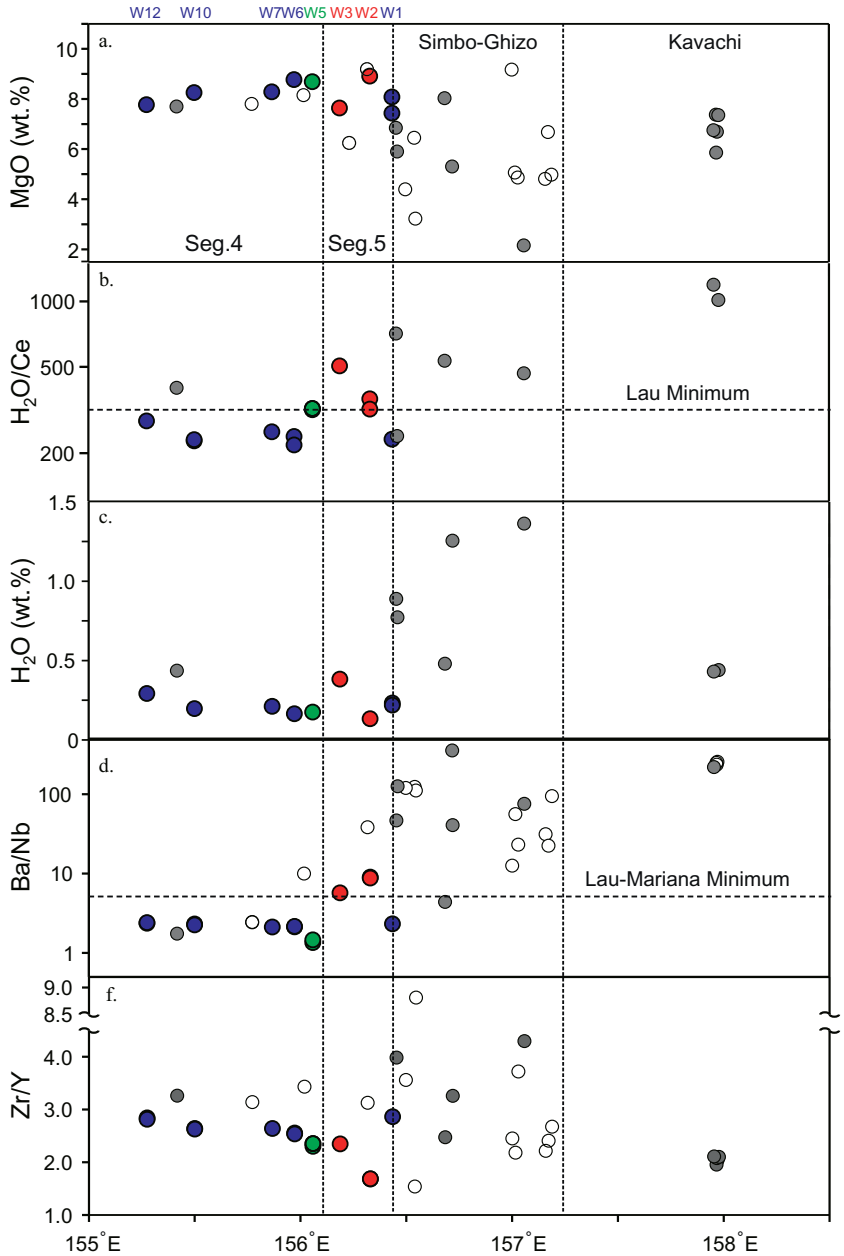

Fig. 5. Along-axis variations in MgO, H_2O, and selected incompatible element ratios. Data for Ghizo and Simbo ridges, Kavachi volcano, and previous studies of the eastern Woodlark Basin are also included where available (white circles = Chadwick et al., 2009; gray circles = Johnson et al., 1987). a) Along-axis variation in MgO. EWLBs are more primitive than Ghizo and Kavachi basalts. b, c) Along-axis variations in H_2O/Ce ratios and H_2O contents, respectively. Data for the Lau minimum line are from Michael and Graham (2015). H_2O contents and H_2O/Ce ratios for Ghizo and Simbo ridges and Kavachi volcano are probably minima, because they are H_2O-saturated at their depth of eruption and would have degassed H_2O. Note that the H_2O contents of samples W2, W3, and W5 are similar to N-EWLB, but W2, W3, and W5 have higher H_2O/Ce. d) Along-axis variation in Ba/Nb ratios. Data for the Lau–Mariana maximum line are from Gale et al. (2013). Note that the Ba/Nb ratios for Ghizo Ridge and Kavachi volcano are much higher than those for the EWLBs from our study. e) Along-axis variation in Zr/Y ratios. Samples W2, W3, and W5 are more depleted than the other samples. Zr/Y ratios of Ghizo Ridge are higher than any EWLB, but Zr/Y ratios of Kavachi volcano are lower than most EWLB, apart from sample W2.

concentrations of incompatible trace elements in batch melts are not significantly different from those of accumulated fractional melts (Plank and Langmuir, 1992). Given that the H_2O contents of the basalts are all <0.4 wt%, we did not consider the effects of H_2O, and the melting beneath the EWSC was modeled as similar to that beneath a dry mid-ocean ridge rather than a hydrous back-arc basin (e.g., Asimow and Langmuir, 2003; Bézos et al., 2009; Kelley et al., 2006; Stolper and Newman, 1994). In addition, the low and constant Dy/Yb ratios (~1.6; Table 1) of the N-EWLB indicate that residual garnet did not strongly influence trace elements during melting beneath the EWSC.

The best model fit for the observed variations in La/Sm versus Zr/Y was obtained by a melting trajectory that starts from a source that underwent 0.5% melt depletion (Fig. 8). According to this model, N-EWLB could have formed by 5%–6% melting of a depleted mantle source that had previously experienced 0.5% melt depletion. Notably, Sr–Nd–Pb isotopic data are not very depleted relative to the global N-MORB range (Fig. 6b and d). This implies that the depletion event in the N-EWLB source was not particularly old.

4.2. VD-EWLB (sample W5)

According to the melting model and Zr/Y versus La/Sm data (Fig. 8), sample W5 could have been produced from a similar source as N-EWLB, but with a factor of two increase in the degree of partial melting.

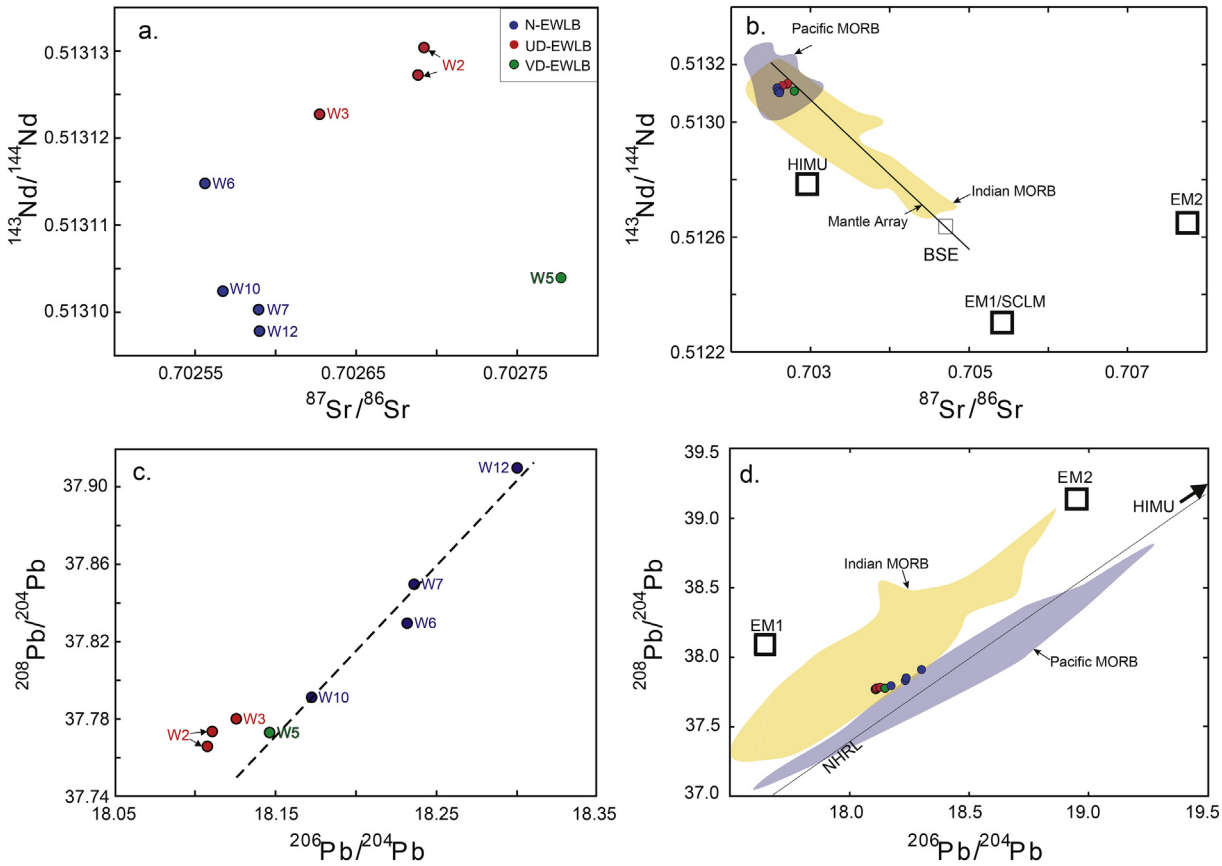

Fig. 6. Sr–Nd–Pb isotopic characteristics of eastern Woodlark Basin basalts. a) $^{87}Sr/^{86}Sr$ versus $^{143}Nd/^{144}Nd$. b) $^{87}Sr/^{86}Sr$ and $^{143}Nd/^{144}Nd$ variations of EWLB in a global context (modified from Park et al., 2006 and references therein). Data for samples W2, W3, and W5 do not define any trend from N-EWLB towards well-known mantle components such as HIMU, EM1, and EM2. c) $^{208}Pb/^{204}Pb$ versus $^{206}Pb/^{204}Pb$. d) Pb isotope variations in a global context.

However, VD-EWLB have distinct geochemical characteristics as compared with N-EWLB, which cannot be explained by differences in the degree of partial melting. Firstly, VD-EWLB have higher $^{87}Sr/^{86}Sr$ at a given $^{143}Nd/^{144}Nd$ relative to N- and UD-EWLB. Secondly, incompatible trace element patterns of VD-EWLB are different to those of N- and UD-EWLB. For example, the combination of high Nb/La and Sm/La in VD-EWLB relative to N-EWLB is unusual in global MORB, given that Nb is more incompatible and Sm is less incompatible than La during peridotite melting. As such, data for MORB almost always show a negative correlation between Nb/La and Sm/La (e.g., Kelemen et al., 2003). Fig. 4f shows that the positive Nb/La–Sm/La trend exhibited by VD- and N-EWLB crosscuts the negative trend defined by global MORB.

To better understand the Nb/La variations in EWLB, we compared Nb_{68} and La_{68} (i.e., Nb and La concentrations corrected for fractionation to Mg# = 68) with Sm/La (Fig. 9). Nb_{68} is constant but La_{68} decreases with increasing Sm/La (Fig. 9) when comparing N-EWLB with sample W5 (VD-EWLB). This indicates that the higher Nb/La in VD-EWLB is due to low La at a relatively constant Nb. This is distinctive because trends of increasing Nb/La ratios in MORB usually result from enrichment of Nb relative to La. The observed EWLB trend could be produced by an eclogitic source containing residual rutile after low-degree melting. Given that Nb is compatible and La is highly incompatible in rutile, Nb/La ratios increase in residual eclogite with progressive melting and depletion (e.g., Kelemen et al., 2003). As such, we propose that the mantle source of VD-EWLB contains residual eclogite.

Other geochemical characteristics also support the above hypothesis. Major element characteristics of VD-EWLB, particularly higher Al_2O_3 and FeO at a given MgO in sample W5 as compared with N-EWLB, can be explained by an eclogitic source, as this would have a basaltic composition that is higher in Al_2O_3 and FeO than peridotite (Fig. 2b and e; Table 1; e.g., Gaetani et al., 2008). Given that eclogite consists of garnet and pyroxene as well as rutile (e.g., Gaetani et al., 2008), a residual garnet signal should also be observed in VD-EWLB for the eclogite hypothesis to be plausible. For example, Zr/Y and Dy/Yb should be low in VD-EWLB, because Y and Yb are more compatible in garnet than are Zr and Dy (e.g., Kelemen et al., 2003). The Zr/Y and Dy/Yb ratios of VD-EWLB (sample W5) are 2.33 and 1.59, respectively, and slightly lower than the average ratios of 2.69 (Zr/Y) and 1.64 (Dy/Yb) for N-EWLB (Table 1; Figs 4 and 5). These differences are also consistent with our hypothesis, although they are less pronounced than the Nb/La enrichment.

Our data also show that VD-EWLB are characterized by relatively high $^{87}Sr/^{86}Sr$ and Sr/Nd (16–16.5) ratios at a given $^{143}Nd/^{144}Nd$ compared with N-EWLB and All-MORB (12.3; Gale et al., 2013). This is also consistent with an eclogite hypothesis, because eclogite in the mantle is generally considered to originate from subducted altered oceanic crust that has high $^{87}Sr/^{86}Sr$ and Sr/Nd ratios due to Sr addition from seawater (Staudigel et al., 1995, 1996). The eclogite hypothesis may also explain other geochemical characteristics of VD-EWLB. Linear trends for VD- and N-EWLB data in Ba/La versus Nb/La and Sm/La versus Nb/La plots might imply that fragments of partially depleted residual eclogite are present in the local upper mantle.

We propose a two-stage process to produce VD-EWLB in the eastern Woodlark Basin. The first stage involved low-degree partial melting of eclogite, which had previously formed by metamorphism of subducted altered oceanic crust (Gaetani et al., 2008; Peacock, 2003). This increased the Nb/La and decreased the Zr/Y and Dy/Yb ratios in the residual eclogite. The second stage involved re-melting of this high-Nb/La, rutile-bearing eclogite beneath the WSC. In this stage, the rutile was

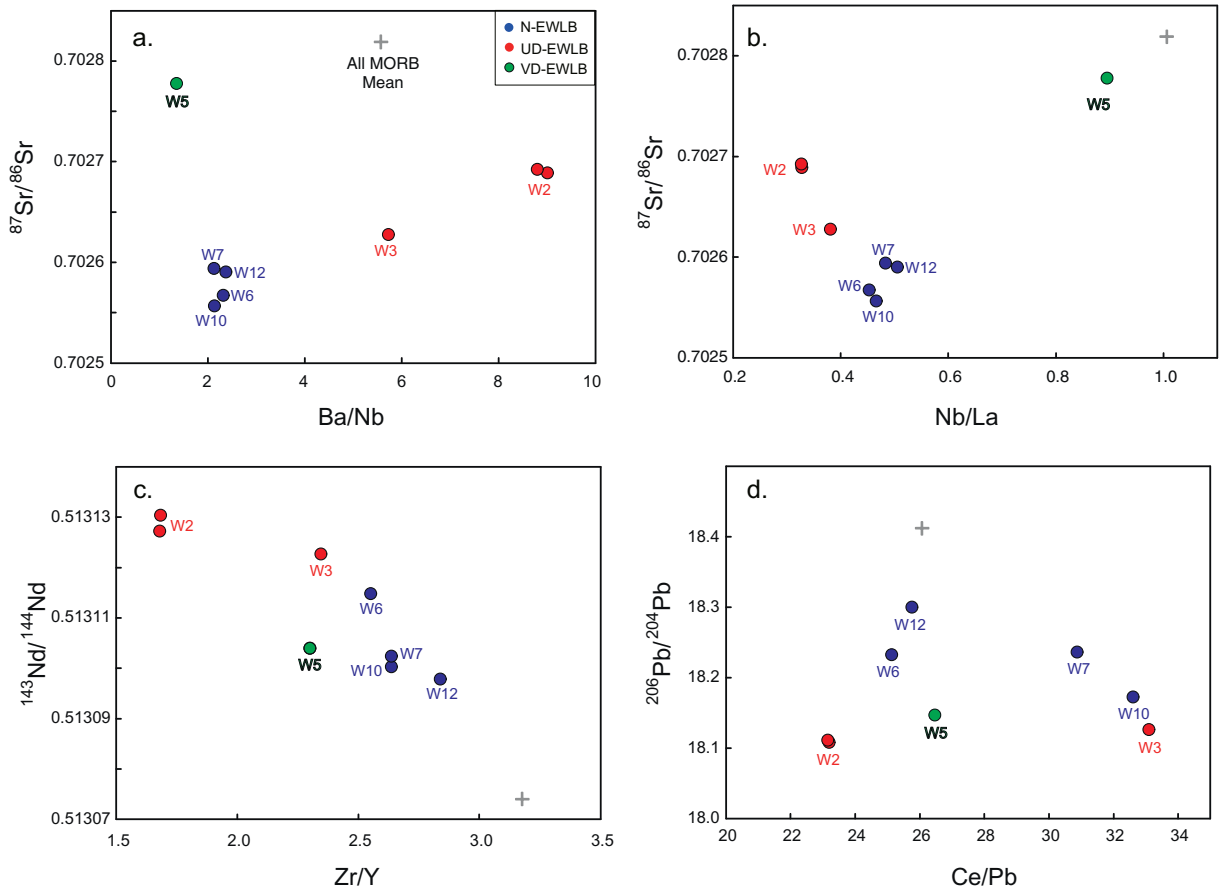

Fig. 7. Relationships between radiogenic isotope data and selected incompatible trace element ratios. Differences in incompatible trace element ratios are correlated with isotopic data. a) $^{87}Sr/^{86}Sr$ versus Ba/Nb. b) $^{87}Sr/^{86}Sr$ versus Nb/La. This diagram shows a negative correlation defined mainly by samples W2 and W3. W5 has high Nb/La and $^{87}Sr/^{86}Sr$. c) $^{143}Nd/^{144}Nd$ versus Zr/Y. d) $^{206}Pb/^{204}Pb$ versus Ce/Pb.

exhausted such that the high-Nb/La source characteristics were transferred to the VD-EWLB. The second stage might have involved 30%–50% partial melting of eclogite (Klemme et al., 2002).

4.3. UD-EWLB (samples W2 and W3)

UD-EWLB are more depleted than N- and VD-EWLB (Figs 3 and 4). The ultra-depleted character of UD-EWLB could have been produced by a higher degree of partial melting of a similar source as N-EWLB. However, based on the modeling shown in Fig. 8, the expected increase in the degree of partial melting would be unrealistically large for sample W2 (5% increasing to 25% partial melting), assuming that UD-EWLB melts were derived from the same source as N-EWLB. If the degree of partial melting was this much higher in the center of Segment 5 (W2 sample location), then the crust would be about four times thicker there. However, geophysical observations show that the variation in crustal thickness along the EWSC is negligible (Martinez et al., 1999), suggesting that the degree of partial melting was not unusually high beneath the W2 sampling site. Therefore, a more reasonable hypothesis is that the source of UD-EWLB was highly depleted as compared with the source of N-EWLB. Moreover, the UD-EWLB have highly incompatible trace element ratios and Sr–Nd–Pb isotopic features that are slightly different to those of N-EWLB, suggesting that this highly depleted mantle had a different origin than the N-EWLB source.

The subduction fingerprints in UD-EWLB provide insights into its origin. These signals are subtle relative to the subduction enrichments in BABB, but are significant because, for example, the Ba/Nb ratio of sample W2 is greater than the lower limit of Lau–Mariana BABB (Figs 4 and 5). Furthermore, the Cl/K_2O ratio of sample W2 (0.138) is much higher than that of N-MORB (0.01–0.02) (Michael and Cornell, 1998). This high Cl/K_2O ratio could be interpreted either as a subduction signal or as resulting from assimilation. Brine assimilation cannot be completely ruled out as the cause of the elevated Cl in sample W2. However, it cannot account for the high H_2O/Ce ratio of sample W2. Even if 75% of the Cl in sample W2 is from assimilation of a 50% NaCl brine (a typical assimilant; Michael and Cornell, 1998), it would only add 0.003 wt% H_2O, which would not significantly change the H_2O/Ce ratio.

Notably, the elemental enrichment in UD-EWLB is different from BABB. For example, BABB have very high H_2O/Ce, Ba/Nb, Ba/La, and Pb/Ce ratios as compared with MORB, and are also high in H_2O and Ba at a given MgO. However, sample W2 has low H_2O at a given MgO content relative to N-EWLB, even though it has high Ba/Nb and H_2O/Ce similar to some BABB. In addition, Ba/La ratios at a given Nb/La and Ce/Pb are close to the mean MORB value.

The subduction fingerprint in BABB can be explained by metasomatic processes, whereby fluids from the subducting slab have increased the concentration of H_2O and fluid-mobile elements and ratios such as H_2O/Ce, Ba/Nb, Ba/La, and Pb/Ce in the source (e.g., Kelley et al., 2010; Langmuir et al., 2006; McCulloch and Gamble, 1991; Miller et al., 1994). Since BABB are formed by melting of this metasomatized source, they have high H_2O/Ce, Ba/Nb, Ba/La, and Pb/Ce ratios, and high contents of H_2O, Ba, and Pb (Class et al., 2000; Gurenko et al., 2016; Kamenetsky et al., 2010; Kelley et al., 2005). However, this process cannot explain the low abundances of H_2O, Ba, and Pb in UD-EWLB relative to BABB.

We propose the following model to explain the subduction fingerprint in UD-EWLB. As described above, the metasomatized source

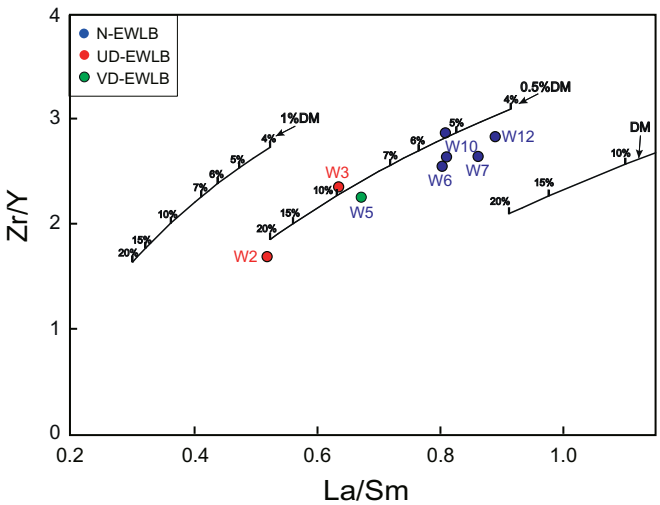

Fig. 8. Mantle melting model in a plot of Zr/Y versus La/Sm. The diagram shows melting trajectories (green lines) from various sources formed by prior depletion (0%, 0.5%, and 1.0%) of depleted mantle (DM) of Salters and Stracke (2004). Prior depleted sources were calculated from DM using the fractional melting equation (Johnson et al., 1990; Shaw, 1970). We used the fractional melting equation to calculate the composition of prior depleted sources, based on evidence from residual abyssal peridotites (Johnson et al., 1990). We used the batch melting equation to calculate melting trajectories from the residues, because batch and accumulated fractional melts have similar concentrations (Plank and Langmuir, 1992). The bulk distribution coefficients of Zr, Y, La, and Sm used in the melting calculations were 0.0276, 0.0869, 0.0077, and 0.0537, respectively. The modal composition of the peridotite that was used to calculate the bulk distribution coefficients is 18% cpx, 30% opx, and 52% olivine (Hirschmann and Stolper, 1996). The distribution coefficients for cpx, opx, and olivine are from Kelemen et al. (2003).

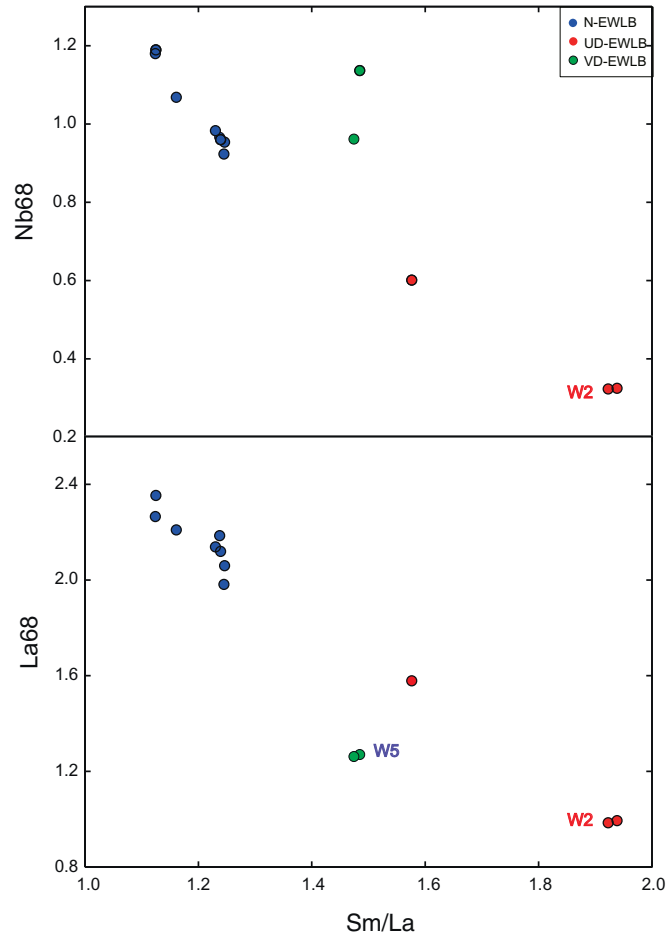

Fig. 9. Nb_{68} and La_{68} versus Sm/La. a) Nb_{68} versus Sm/La. b) La_{68} versus Sm/La. Nb_{68} and La_{68} were calculated by multiplying the Nb and La concentrations (in ppm) by F, which is the fraction of liquid remaining after crystallization from a parental magma having Mg# = 68 [Mg# = 100 × Mg/(Mg + Fe^{2+}), with $Fe^{2+} = 0.9 \times Fe_{(total)}$; all values are molar]. The calculation of Nb_{68} and La_{68} assumes that the bulk distribution coefficients for Nb and La during crystallization are zero. Slightly higher bulk distribution coefficients make a negligible difference to our calculations. F = (100– percent crystallized)/100. The "percent crystallized" was calculated using a regression equation for Mg# versus "percent crystallized" that was derived from least-squares mixing calculations of major elements in suites of MORBs that closely follow liquid lines of descent with very low residuals (Michael and Graham, 2015).

beneath the back-arc (arc) shows high H_2O/Ce, Ba/Nb, Ba/La, and Pb/Ce ratios, and high H_2O, Ba, and Pb contents. However, melting of this metasomatized source would leave the residual mantle low in H_2O, Ba, and Pb contents, because these are incompatible species/elements. Ba/Nb ratios would decrease to a much lesser extent than these elemental and H_2O concentrations because Nb is highly incompatible and also prefers to enter the melt (e.g., Kelemen et al., 2003). Water and Ce are also similarly incompatible during melting (Michael, 1995), and so the H_2O/Ce ratio in the residual mantle will decrease less than the H_2O or Ce contents. As such, the residual mantle would retain a subduction fingerprint for Ba/Nb and H_2O/Ce ratios. However, La is less incompatible than Nb, and Ba becomes more incompatible during wet melting than dry melting (e.g., Kelemen et al., 2003). Therefore, Ba/La ratios would be much lower in the residual mantle than in the melt. Cerium is similarly incompatible to Pb during dry melting, but Pb becomes highly incompatible during wet melting. As such, Pb/Ce ratios in the sub-arc residual mantle should be much lower than in BABB (e.g., Kelemen et al., 2003). In summary, residual mantle that had been metasomatized by fluid components and then had melts extracted would have high Ba/Nb and H_2O/Ce ratios, and low Ba and H_2O contents, similar to the subduction fingerprint in UD-EWLB. Therefore, we suggest that the ultra-depleted mantle that formed the UD-EWLB might be sub-arc residual mantle. A linear relationship between UD- and N-EWLB data in Ba/La versus Nb/La and Sm/La versus Nb/La diagrams can be interpreted as mixing between sub-arc residual mantle and local upper mantle (or between melts produced by each source).

The positive correlation between $^{143}Nd/^{144}Nd$ and $^{87}Sr/^{86}Sr$ for UD- and N-EWLB is unusual. Given that UD-EWLB are more depleted in incompatible trace elements than N-EWLB, the higher $^{143}Nd/^{144}Nd$ of UD-EWLB might be the result of time-integrated effects of higher Sm/Nd. The relatively high Sr/Ce ratio (17–18) of sample W2 compared with All MORB (8.68) and N-MORB (10.3) (Gale et al., 2013; Sun and McDonough, 1989), as well as N-EWLB, may reflect a subduction input. $^{87}Sr/^{86}Sr$ ratios are typically elevated in subduction components (Class et al., 2000), and so the higher $^{87}Sr/^{86}Sr$ in UD-EWLB could be interpreted as a subduction signal. UD-EWLB are also characterized by low $^{206}Pb/^{204}Pb$ ratios relative to N-EWLB. Lead is also supplied in subduction components, which typically have high $^{206}Pb/^{204}Pb$. However, UD-EWLB are very low in Pb and Pb/Ce, similar to N-MORB, suggesting that fluid-mobile Pb in the sub-arc mantle was almost entirely removed by partial melting.

4.4. Origins of the subduction fingerprints beneath the eastern Woodlark Basin

Determining the origin of the subduction signals in the Woodlark Basin samples is not straightforward because this basin is not part of an overriding plate below which the subduction components are supplied from an identifiable slab. In fact, the Woodlark Basin is part of a subducting plate. Based on the tectonic history of the region, three possible origins for the subduction fingerprint are possible: the current ridge subduction via a slab window (Chadwick et al., 2009); previous long-term subduction of the stalled Pacific Plate (Johnson et al., 1987;

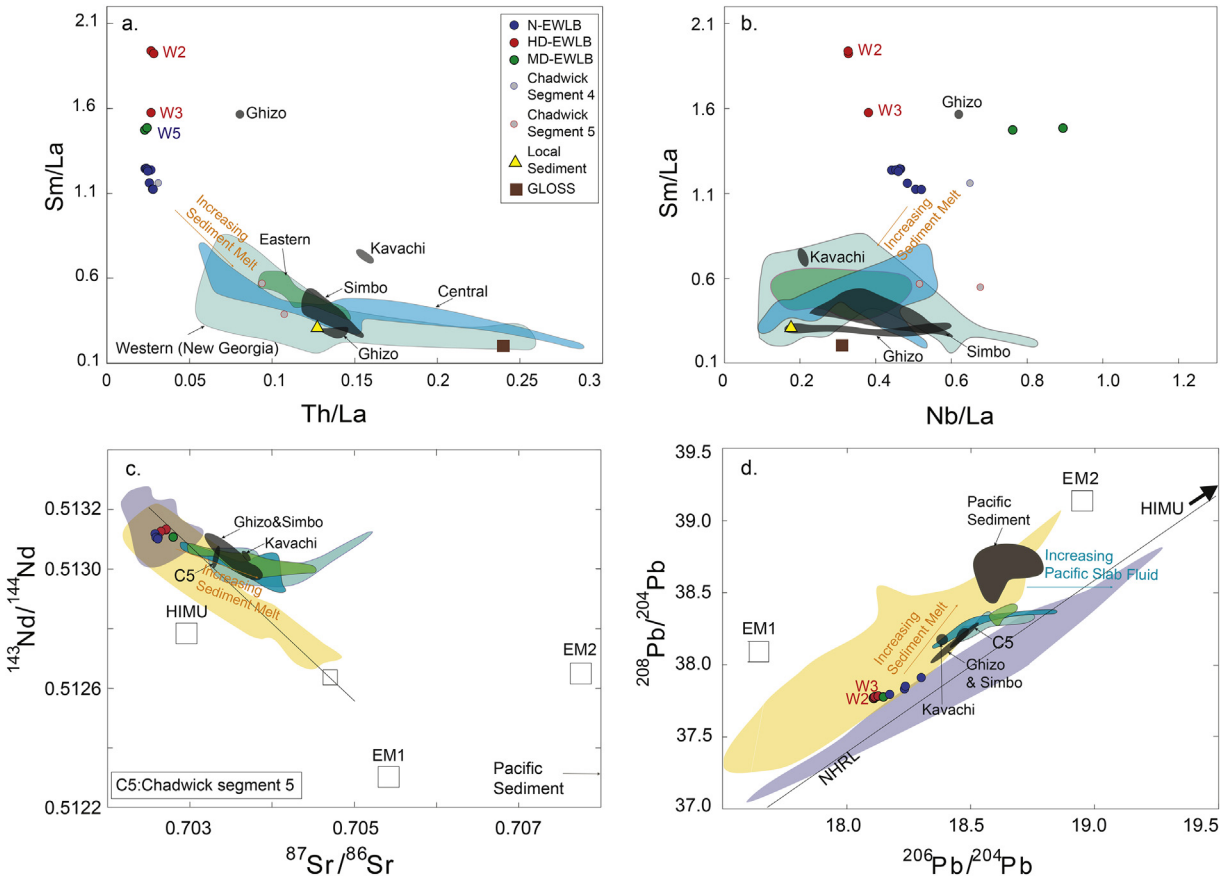

Fig. 10. Comparisons of data for the EWLB with those for the Solomon Arc and Ghizo–Simbo ridges. Data fields for the western, central, and eastern Solomon Arc are based on data from Schuth et al. (2011), König and Schuth (2011), and Schuth et al. (2009). Kavachi volcano, and Ghizo and Simbo ridge data are from Chadwick et al. (2009). GLOSS and local sediment (Vanuatu) data are from Plank and Langmuir (1998). GLOSS is representative of subducted sediment. Vanuatu is somewhat distant (to the west) from the New Georgia Arc, but is very close to the eastern Solomon Arc. We were unable to find any data closer to the WSC than those for Vanuatu. The Pacific sediment field is from Hegner and Smith (1992). a) Sm/La versus Th/La. The trend produced by mixing of a sediment melt is indicated by arrows. Simbo and Ghizo ridges are geochemically similar to the Solomon Arc. b) Sm/La versus Nb/La. This diagram shows similar variations as for Sm/La versus Th/La. c) $^{87}Sr/^{86}Sr$ versus $^{143}Nd/^{144}Nd$. Samples W2 and W3 have slightly elevated $^{87}Sr/^{86}Sr$, and trend away from data for the Solomon Arc, which has lower $^{143}Nd/^{144}Nd$, as compared with N-EWLB. d) $^{208}Pb/^{204}Pb$ versus $^{206}Pb/^{204}Pb$. This diagram shows that the variations in the Solomon Arc might be explained by involvement of a sediment melt and Pacific-slab-derived fluid.

Perfit et al., 1987); and Paleogene subduction of the Indo-Australian Plate.

Chadwick et al. (2009) suggested there was a "slab window" in the subducting plate, through which the subduction components beneath the Solomon Arc were transported to the mantle beneath the eastern Woodlark Basin. This proposal was based on several samples from Segment 5 and the Ghizo and Simbo ridges that have strong subduction signatures, and which are geochemically similar to the New Georgia Group in the Solomon Arc. However, the subtle subduction fingerprints we observe (in VD- and UD-EWLB) are different from those in any region of the Solomon Arc or the Ghizo and Simbo ridges. Firstly, Th/La, which is a sediment melt tracer (Plank, 2005) is lower in the EWLB than in the Solomon Arc lavas (Fig. 10a). Secondly, relative to the ambient local mantle (N-EWLB), the Nb/La ratio of sample W5 trends in the opposite direction to data for samples from the Solomon Arc (Fig. 10b). Thirdly, $^{143}Nd/^{144}Nd$ ratios of UD-EWLB are higher than those of N-EWLB and trend in the opposite direction to data from the Solomon Arc (Fig. 10c). Finally, the Pb isotopic trends of samples W2, W3, and W5 vector in different directions than data for the Solomon arc, which plot towards sediment and Pacific-type Pb isotopic compositions (Fig. 10d; Schuth et al., 2009, 2011). In addition, the H_2O/Ce and Ba/Nb ratios and H_2O content of sample W1, located on the easternmost part of Segment 5, are low (as for N-MORB), even though W1 is closer to the ridge subduction zone than VD- and UD-EWLB (Figs 1 and 5). In summary, the VD- and UD-EWLB are not simply a diluted expression of the geochemical characteristics of the Solomon Arc (Fig. 10). Similarly, the stalled Pacific Plate (Perfit et al., 1987) can be ruled out as a source of VD- and UD-EWLB on the basis of Pb isotope data (Fig. 10d). Therefore, the subduction fingerprints in samples W2, W3, and W5 are difficult to relate to the current subduction or earlier, long-term subduction of the stalled Pacific Plate.

The trajectories of the Pb isotopic data for VD- and UD-EWLB away from N-EWLB are much better explained by input from an Indian-type slab source (Fig. 10d). If we consider that the Woodlark Basin was developed on a remnant arc that was generated during Paleogene subduction of the Indo-Australian Plate, it is not surprising that the source of EWLB lavas would contain Paleogene subduction components. Based on these observations, we propose that the sources of EWLB lavas include the eclogitic slab and contaminated mantle wedge material from Paleogene subduction of the Indo-Australian Plate. We speculate that the mantle beneath the New Guinea Arc has become rigid and fixed at a certain depth after the cessation of Paleogene subduction. This sub-arc mantle included subducted oceanic crust, which was then reactivated after spreading of the Woodlark Basin began. Denser sampling and geochemical data are required from the eastern Woodlark Basin and New Guinea Arc to test this hypothesis.

5. Conclusions

Highly depleted basalts from the eastern Woodlark Basin, including VD- and UD-EWLB, might have been derived from residual mantle sources that were depleted by subduction processes. VD- and UD-EWLB

might be derived from mantle containing fragments of sub-arc residual mantle and residual eclogite, respectively.

The subduction fingerprints in VD- and UD-EWLB are geochemically different from the Solomon Arc, which is strongly influenced by the current ridge subduction and/or earlier, long-term subduction of the Pacific Plate. This suggests that the VD- and UD-EWLB sources are not related to these two subduction events. The subduction fingerprints were most likely generated during Paleogene subduction of the Indo-Australian Plate to the south of the Woodlark Basin.

Acknowledgments

SHP thanks the crew members of R/V Onnuri for dredging during the severe sea conditions during the cruise. This work is supported by a grant from the Korea Polar Research Institute (PP13040 and PE18050). The paper started as a part of Ph.D program for SHP. PJM acknowledges support of the US National Science Foundation (OCE0752255, OCE0752256) and the McMan endowment of the University of Tulsa.

Appendix A. Analytical methods

All analyses were made on hand-picked fresh basalt glasses. Detailed analytical methods for major, trace, volatile and Sr-Nd-Pb isotopes are as follows.

A.1. Major elements

Natural basalt glasses were analyzed for all major elements using the automated four spectrometer Cameca microprobe at the University of Tulsa. Several fragments from various parts of each sample were cleaned ultrasonically in distilled water and then were handpicked. Accelerating voltage was 15 kV, beam current was 25 nA, and a 20-μm beam diameter was used. On-peak counting times were 10 s for Si; 20 s for Al; 30 s for Na, Mg and Mn; 40 s for P; 50 s for Ca and Ti; 60 s for K and 70s for Fe. Backgrounds were obtained at interference-free wavelengths on either side of the peak using one half the counting time as peaks. Natural mineral standards were used and all analyses are normalized to Hawaiian basaltic glass VG-A99 and Kakanui augite (Jarosewich et al., 1980), which were run concurrently with the unknowns. Each analysis is the average of at least four spot analyses.

A.2. Trace elements

Glass fragments were handpicked using a stereomicroscope avoiding chips with phenocrysts, microlites, and heavily MnO-encrusted and/or altered fragments. These were ultrasonically cleaned in a 60:40 solution of 1.4 N HCl (trace metal grade) and 30% H_2O_2. After insonification, approximately 50 mg of the cleanest glass chips were handpicked and placed in pre-cleaned 7 ml Teflon Savillex© vials. Glass chips were digested with HF + HHO_3, dried down, refluxed overnight with 6 N HCl to convert insoluble fluorides to chlorides and then evaporated to a soluble residue. Optima-grade acids were used in all leaching, digestion, and analytical procedures. Residues were diluted with ~ 4.5 ml of 5% HNO_3 + 0.01% HF spiked with 8 ppb each of Re and Rh, capped and refluxed on a hotplate overnight. Similarly, 4.5 ml of an unspiked HNO_3 – HF mixture was added to a procedural blank that was prepared with each batch of samples to monitor acid purity and lab contamination. Unknowns were diluted 2000× and analyzed in medium resolution mode for 34 trace elements on a high-resolution magnetic-sector Element 2 Inductively Coupled Plasma Mass Spectrometer (ICP-MS) at the University of Florida, Department of Geological Sciences. Re and Rh were used as an internal standard to correct for instrumental drift and matrix effects. Blanks were subtracted from the count totals, and quantification of the results was done by external calibration using a combination of USGS (AGV-1, BIR-1, BHVO-1, BCR-1) and internal (ENDV–Endeavour) rock standards. Instrumental drift, as well as data accuracy and long-term reproducibility were assessed by sequential analyses ($n = 9$) of a secondary internal standard, ALV2392. External long-term reproducibility is <5% for all trace elements. Due to the low Pb concentration, several samples (W2–1, W3–2, W5–2 and W12–1) were spiked with UF1a ^{208}Pb spike and Pb concentrations were determined with isotope dilution (ID). The Pb isotope measurements for the ID were performed on a Nu-Plasma MC-ICP-MS with Tl used as an internal standard. For more details see Kamenov et al. (2008).

A.3. Volatiles

Chlorine, fluorine, sulfur, potassium and titanium were analyzed simultaneously using the four spectrometer Cameca microprobe at the University of Tulsa. Glasses were analyzed using a 15 kV beam and 80 nA beam current with a 20 μm beam diameter. Peak positions were counted for 200 s, while background positions on either side of the peak were counted for 100 s each (80 s on potassium; 20 s on titanium). We verified that the intense beam did not alter the glass during the analyses and lead to compositional or count rate changes of the elements by checking several glasses for count rate variations over consecutive 20 s intervals. Reported analyzes are the average of four individual spots. Two-sigma precision, based on multiple three-spot analyses of the same basalts glass, are ±0.003% for Cl, ±0.013% for F and ± 0.005% for S. Standards were: natural scapolite for Cl, synthetic F-phlogopite for F, and pyrite for S. Instrument drift was monitored using frequent analyses of a secondary standard: TR154 21D3. Concentrations of H_2O and CO_2 dissolved in glasses were analyzed by Fourier Transform Infrared Spectroscopy at the University of Tulsa using published methods and calibrations (Dixon et al., 1988, 1995) with slight modifications (Michael, 1995). Doubly polished glass wafers, 100-250 μm thick, were placed atop a 2 mm thick KBr pellet and analyzed using a NicPlan IR microscope equipped with a HgCdTe detector, attached to a Nicolet 520 FTIR. Thickness was measured by two methods: first by digital micrometer, and secondly by focusing the calibrated z-axis of the FTIR microscope stage on the glass wafer and on the adjacent KBr disk using reflected light. Optically clear areas of known thickness (± 2 μm), 80 × 80 μm, were analyzed with 256 scans/spot. Absorbance at the broad 3550 cm-1 (combined OH and H_2O) and 1630 cm^{-1} (molecular H_2O only) peaks were measured after subtraction of interpolated backgrounds. Density was assumed to be 2.8 g/cm^3. Molar absorption coefficients used for all glasses were: 63 l/mol-cm for 3550 and 25 l/mol cm for e1630. Analyses are the average of 3–4 spot determinations of 3550 cm^{-1} on two separate wafers. Replicate analyses of different wafers from the same specimen were typically reproducible to ±5%. All CO_2 is present as dissolved CO_3^{2-}, which appears as an absorbance doublet at 1435 and 1515 cm^{-1} (Fine and Stolper, 1986). Estimation of the complex background in this region is often the largest source of analytical error, so the spectrum of a volatile-free reference glass from Juan de Fuca Ridge (Dixon et al., 1988) was subtracted from each sample spectrum and the background of the resulting spectrum was determined using a spreadsheet designed for FTIR curve fitting of basalt glasses (S. Newman, personal communication). Concentrations at the low levels of Woodlark glasses are reproducible to about ±15 ppm CO_2.

A.4. Sr-Nd-Pb analysis

Sample dissolution and element chromatography were carried out at GEOMAR Helmholtz Centre for Ocean Research in Class 1000 clean rooms, equipped with Class 100 laminar flow hoods. Sr-Nd-Pb isotope analyses were carried out on fresh glass chips that were leached in 2 N HCl at 70 °C for 60 min and triple rinsed in ultra pure H_2O prior to dissolution. About 200 mg of sample were weighed into a Teflon beaker and then dissolved for 2 days in a 5:1 mixture of HF and HNO_3 at 150 °C. The ion chromatography followed established standard procedures (Hoernle et al., 2008). Isotopic ratios were determined by thermal

ionization mass spectrometry (TIMS) at GEOMAR on a TRITON (Sr—Nd) and MAT262 RPQ2+ TIMS (Pb). Both instruments operate in static multi-collection mode. Sr and Nd isotopic ratios are normalized for each integration to $^{86}Sr/^{88}Sr = 0.1194$ and $^{146}Nd/^{144}Nd = 0.7219$ respectively and all errors are reported as 2 sigma of the mean. Reference material measured along with the samples gave $^{87}Sr/^{86}Sr = 0.710230 \pm 0.000003$ ($n = 4$) for NBS987 and was normalized to $^{87}Sr/^{86}Sr = 0.710250$. For La Jolla, $^{143}Nd/^{144}Nd = 0.511852 \pm 0.000004$ ($N = 4$) was obtained and normalized to $^{143}Nd/^{144}Nd = 0.511850$. Pb isotope ratios were determined using a Pb double-spike technique described in Hoernle et al. (2011). At the time the sample data were generated the long-term reproducibility of double spike corrected NBS981 values ($n = 44$) was $^{206}Pb/^{204}Pb = 16.9425 \pm 0.0025$, $^{207}Pb/^{204}Pb = 15.4999 \pm 0.0024$, $^{208}Pb/^{204}Pb = 36.7237 \pm 0.0066$ and compare well with published (e.g. Baker et al., 2004; Galer and Abouchami, 1998; Thirlwall, 2000, 2002) double and triple spike data for NBS981. Replicate analysis of sample W7–2 by means of a separate digestion was reproduced within the above stated errors for the standards. Total chemistry blanks are <50 pg for Sr—Nd and <30 pg for Pb and thus are considered negligible.

Appendix B. Supplementary data

Supplementary data to this article can be found online at https://doi.org/10.1016/j.lithos.2018.07.003.

References

Asimow, P.D., Langmuir, C.H., 2003. The importance of water to oceanic mantle melting regime. Nature 421, 815–820.

Baker, J., Peate, D., Waight, T., Meyzen, C., 2004. Pb isotopic analysis of standards and samples using a ^{207}Pb-^{204}Pb double spike and thallium to correct for mass bias with a double-focussing MC-ICP-MS. Chem. Geol. 211, 275–303.

Bézos, A., Escrig, S., Langmuir, C.H., Michael, P.J., Asimow, P.D., 2009. Origins of chemical diversity of back-arc basin: a segment-scale study of the Eastern Lau Spreading Center. J. Geophys. Res. 114:B06212. https://doi.org/10.1029/2008JB005924.

Chadwick, J., Perfit, M., McInnes, B., Kamenov, G., Plank, T., Jonasson, I., 2009. Arc lavas on both sides of a trench: Slab window effects at the Solomon Islands triple junction, SW Pacific. Earth Planet. Sci. Lett. 279, 292–302.

Class, C., Miller, D.M., Goldstein, S.L., Langmuir, C.H., 2000. Distinguishing melt and fluid subduction components in Umnak Volcanics, Aleutian Arc. Geochem. Geophys. Geosyst. 1, 1999GC000010.

Cooper, P., Taylor, B., 1985. Polarity reversal in the Solomon Island arc. Nature 314, 428–430.

Danyushevsky, L.V., 2001. The effect of small amounts of H_2O on crystallisation of mid ocean ridge and backarc basin magmas. J. Volcanol. Geotherm. Res. 110, 265–280.

Danyushevsky, L.V., Plechov, P., 2011. Petrolog3: integrated software for modeling crystallization processes. Geochem. Geophys. Geosyst. 12, Q07021.

Devey, C.W., 2009. Magma genesis, tectonic and hydrothermalism in the Woodlark Basin. Cruise Report SO203 Woodlark (169 pp).

Dixon, J.E., Stolper, E., Delaney, J.R., 1988. Infrared spectroscopic measurements of CO_2 and H_2O in Juan de Fuca Ridge basaltic glasses. Earth Planet. Sci. Lett. 90, 87–104.

Dixon, J.E., Stolper, E.M., Holloway, J.R., 1995. An experimental study of water and carbon dioxide solubilities in midocean ridge basaltic liquids, part I, Calibration and solubility models. J. Petrol. 36, 1607–1631.

Faure, G., 1986. Principles of Isotope Geology. Wiley (608pp).

Fine, G., Stolper, E., 1986. CO_2 in basaltic glasses: Concentration and speciation. Earth Planet. Sci. Lett. 76, 263–278.

Gaetani, G.A., Asimow, P.D., Stolper, E.M., 2008. A model for rutile saturation in silicate melts with applications to eclogite partial melting in subduction zones and mantle plumes. Earth Planet. Sci. Lett. 272, 720–729.

Gale, A., Dalton, C.A., Langmuir, C.H., Su, Y., Schilling, J.G., 2013. The mean composition of ocean ridge basalts. Geochem. Geophys. Geosyst. 14. https://doi.org/10.1029/2012GC004334.

Galer, S.J.G., Abouchami, W., 1998. Practical application of lead triple spiking triple spiking for correction of instrumental mass discrimination. Mineral. Mag. 62A, 491–492.

Gill, J.B., 1976. Comparison and age of Lau Basin and Ridge volcanic rocks: implications for evolution of an interarc basin and remnant arc. Geol. Soc. Am. Bull. 87, 1295–1384.

Goodliffe, A.M., Taylor, B., Martinez, F., Hey, R.N., Maeda, K., Ohno, K., 1997. Synchronous reorientation of the Woodlark Basin spreading center. Earth Planet. Sci. Lett. 146, 233–242.

Gurenko, A.A., Kamenetsky, V.S., Kerr, A., 2016. Oxygen isotopes and volatile contents of the Gorgona komatiites, Colombia: a confirmation of the deep mantle origin of H2O. Earth Planet. Sci. Lett. 454, 154–165.

Hegner, E., Smith, E.M., 1992. Isotopic compositions of late Cenozoic volcanics from southeast Papua New Guinea: Evidence for multi-component sources in arc and rift environment. Chem. Geol. 97, 233–249.

Hirschmann, M.M., Stolper, E.M., 1996. A possible role for garnet pyroxenite in the origin of the "garnet signature" in MORB. Contrib. Mineral. Petrol. 124, 185–208.

Hoernle, K., Abt, D.L., Fischer, K.M., Nichols, H., Hauff, F., Abers, G.A., van den Bogaard, P., Heydolph, K., Alvarado, G., Protti, M., Strauch, W., 2008. Arc-parallel flow in the mantle wedge beneath Costa Rica and Nicaragua. Nature 451, 1094–1097.

Hoernle, K., Hauff, F., Kokfeit, T.F., Haase, K., Garbe-Schönberg, D., Werner, R., 2011. On- and off-axis chemical heterogeneities along the South Atlantic Mid-Ocean-Ridge (5-11°S): Shallow or deep recycling of ocean crust and/or intraplate volcanism? Earth Planet. Sci. Lett. 306, 86–97.

Jarosewich, E., Nelen, J.A., Norberg, J.A., 1980. Reference samples for electron microprobe analysis. Geostand. Newslett. 4, 43–47.

Johnson, R.W., Jaques, A.L., Langmuir, C.H., Perfit, M.R., Staudigel, H., Dunkley, P.N., Chappell, B., Taylor, S.R., 1987. Ridge subduction and fore-arc volcanism: petrology and geochemistry of rocks dredged from the western Solomon arc and the Woodlark Basin. In: Taylor, B., Exon, N. (Eds.), Marine Geology, Geophysics and Geochemistry of the Woodlark Basin-Solomon Islands. Circum-Pacific Council for Energy and Mineral Resources, Houston, pp. 155–226.

Johnson, K.T.M., Dick, H.J.B., Shimizu, N., 1990. Melting in the oceanic upper mantle: an ion microprobe study of diopsides in abyssal peridotites. J. Geophys. Res. 95, 2661–2678.

Kamenetsky, V.S., Gurenko, A.A., Kerr, A.C., 2010. Composition and temperature of komatiite melts from Gorgona Island constrained from olivine-hosted melt inclusions. Geology 38, 1003–1006.

Kamenov, G.D., Perfit, M.R., Mueller, P.A., Jonasson, I.R., 2008. Controls on magmatism in an island arc environment: study of lavas and sub-arc xenoliths from the Tabar-Lihir-Tanga-Feni island chain, Papua New Guinea. Contrib. Mineral. Petrol. 155, 635–656.

Karig, D.E., 1972. Remnant Arcs. Geol. Soc. Am. Bull. 83, 1057–1068.

Kelemen, P.B., Yogodzinski, G.M., Scholl, D.W., 2003. Along-strike variation in the Aleutian island arc: Genesis of high Mg# andesite and implications for continental crust. In: Eiler, J. (Ed.), Inside the Subduction Factory. Geophysical Monograph Vol. 138, pp. 223–276.

Kelley, K.A., Plank, T., Farr, L., Ludden, J., Staudigel, H., 2005. Subduction cycling of U, Th, and Pb. Earth Planet. Sci. Lett. 234, 369–383.

Kelley, K.A., Plank, T., Grove, T.L., Stolper, E.M., Newman, S., Hauri, E.H., 2006. Mantle melting as a function of water content beneath back-arc basins. J. Geophys. Res. III: B09208. https://doi.org/10.1029/2005JB003732.

Kelley, K.A., Plank, T., Newman, S., Stolper, E.M., Grove, T.L., Parman, S., Hauri, E.H., 2010. Mantle melting as a function of water content beneath the Mariana Arc. J. Petrol. 51 (8), 1711–1783.

Klein, E.M., Karsten, J.L., 1995. Ocean-ridge basalts with convergent-margin geochemical affinities from the Chile Ridge. Nature 374, 27–52.

Klein, E.M., Langmuir, C.H., Zindler, A., Staudigel, H., Hamelin, B., 1988. Isotopic evidence of a mantle convection boundary at the Australian-Antarctic Discordance. Nature 133, 623–629.

Klemme, S., Blundy, J.D., Wood, B.J., 2002. Experimental constraints on major and trace element partitioning during partial melting of eclogite. Geochim. Cosmochim. Acta 66, 3109–3123.

König, S., Schuth, S., 2011. Deep melting of old subducted oceanic crust recorded superchondritic Nb/Ta in modern island arc lavas. Earth Planet. Sci. Lett. 301, 265–274.

Langmuir, C.H., Klein, E.M., Plank, T., 1992. Petrological systematics of mid-ocean ridge basalts: Constraints on melt generation beneath ocean ridges. In: Morgan, J.P., Blackman, D.K., Sinton, J.M. (Eds.), Mantle Flow and Melt Generation at Mid-Ocean Ridges. Geophysical Monograph Series vol. 71. American Geophysical Union, Washington D.C., pp. 183–280.

Langmuir, C.H., Bézos, A., Escrig, S., Parman, S.W., 2006. Chemical systematics and hydrous melting of the mantle in back-arc basins. In: Christie, D.M., Fisher, C.R., Lee, S.-M., Givens, S. (Eds.), Geological, Biological, Chemical, and Physical Interactions. Geophysical Monograph Series vol. 166. American Geophysical Union, Washington D.C., pp. 87–146.

Martinez, F., Taylor, B., Goodliffe, A.M., 1999. Contrasting styles of seafloor spreading in the Woodlark Basin: Indications of rift-induced secondary mantle convection. J. Geophys. Res. 104, 12,909–12,926.

McCulloch, M.T., Gamble, J.A., 1991. Geochemical and geodynamical constraints on subduction zone magmatism. Earth Planet. Sci. Lett. 102, 358–374.

Michael, P.J., 1995. Regionally distinctive sources of depleted MORB: evidence from trace elements and H_2O. Earth Planet. Sci. Lett. 131, 301–320.

Michael, P.J., Cornell, W.C., 1998. Influence of spreading rate and magma supply on crystallization and assimilation beneath mid-ocean ridges: evidence from chlorine and major element chemistry. J. Geophys. Res. 103 (18), 325–18,356.

Michael, P.J., Graham, D.W., 2015. The behavior and concentration of CO_2 in the suboceanic mantle: inferences from undegassed ocean ridge and ocean island basalts. Lithos 236–237, 338–351.

Miller, D.M., Goldstein, S.L., Langmuir, C.H., 1994. Cerium/lead and lead isotope ratios in arc magmas and the enrichment of lead in the continents. Nature 368, 514–519.

Park, S.-H., Lee, S.-M., Arculus, R.J., 2006. The geochemistry of basalt from the Ayu Trough, south ease equatorial Pacific. Earth Planet. Sci. Lett. 248, 700–714.

Peacock, S.M., 2003. Thermal structure and metamorphic evolution of subducting slabs. In: Eiler, J.M. (Ed.), Inside the Subduction Factory. Geophysical Monograph Vol. 138. American Geophysical Union, Washington, D.C, pp. 7–22.

Pearce, J.A., Parkinson, I.J., 1993. Trace Element Models for Mantle Melting: Application to Volcanic Arc Petrogenesis. 76. Geological Society Special Publications, pp. 373–403.

Pearce, J.A., Peate, D.W., 1995. Tectonic implications of the volcanic arc magmas. Annu. Rev. Earth Planet. Sci. 23, 251–285.

Pearce, J.A., Stern, R.J., 2006. Origin of back-arc basin magmas: trace elements and isotope perspective. In: Christie, D.M., Fisher, C.R., Lee, S.-M., Givens, S. (Eds.), Geological, Biological, Chemical, and Physical Interactions. Geophysical Monograph Series vol. 166. American Geophysical Union, Washington D.C., pp. 63–86.
Pearce, J.A., Stern, R.J., Bloomer, S.H., Fryer, P., 2005. Geochemical mapping of the Mariana arc-basin system: implications for the nature and distribution of subduction components. Geochem. Geophys. Geosyst. 6 (2004GC000895).
Perfit, M.R., Langmuir, C.H., Backisapa, M., Chappell, B., Johnson, R.W., Staudigel, H., Taylor, S.R., 1987. Geochemistry and petrology of volcanic rocks from the Woodlark Basin: addressing questions of ridge subduction. In: Taylor, B., Exon, N. (Eds.), Marine Geology, Geophysics and Geochemistry of the Woodlark Basin - Solomon Islands. Circum-Pacific Council for Energy and Mineral Resources, Houston, pp. 113–154.
Pigram, C.J., Symonds, P.A., 1991. A review of the major tectonic events in the New Guinea Orogen. J. SE Asian Earth Sci. 6, 307–318.
Plank, T., 2005. Constraints from Thorium/Lanthanum on sediment recycling at subduction zones and the evolution of the continent. J. Petrol. 46, 921–944.
Plank, T., Langmuir, C.H., 1992. Effects of the melting regime on the composition of the oceanic crust. J. Geophys. Res. 97, 19,749–19,770.
Plank, T., Langmuir, C.H., 1998. The chemical composition of subducted sediment and its consequences for the crust and mantle. Chem. Geol. 145, 325–394.
Salters, V.J.M., Stracke, A., 2004. Composition of the depleted mantle. Geochem. Geophys. Geosyst. 5 (2003GC000597).
Schellart, W.P., Lister, G.S., Toy, V.G., 2006. A late Cretaceous and Cenozoic reconstruction of the Southwest Pacific region: Tectonics controlled by subduction and slab rollback processes. Earth Sci. Rev. 76, 191–233.
Schuth, S., Münker, C., König, S., Qopoto, C., Basi, S., Grabe-Schönberg, D., Ballhaus, C., 2009. Petrogenesis of lavas along the Solomon Island Arc, SW Pacific: couplong of compositional variations and sbuduction zone geometry. J. Petrol. 50, 781–811.
Schuth, S., König, S., Münker, C., 2011. Subduction zone dynamics in SW Pacific plate boundary region constrained from high-precision Pb isotope data. Earth Planet. Sci. Lett. 311, 328–338.
Shaw, D.M., 1970. Trace element fractionation during anatexis. Geochim. Cosmochim. Acta 34, 237–243.
Sinton, J.M., Fryer, P., 1987. Mariana Trough lavas from 18°N: implications for the origin of back-arc basin basalts. J. Geophys. Res. 92 (12), 12,782–12,802.
Staudigel, H., Davies, G.R., Hart, S.R., Marchant, K.M., Smith, B.M., 1995. Large scale isotopic Sr, Nd an O isotopic anatomy of altered oceanic crust: DSDP/ODP sites 417/418. Earth Planet. Sci. Lett. 130, 169–185.
Staudigel, H., Plank, T., White, W., Schminke, H.U., 1996. Geochemical fluxes driving seafloor alteration of the basaltic upper crust: DSDO site 417 and 418. In: Bebout, G.E., Scholl, D.W., Kirby, S.H., Platt, J.P. (Eds.), Subduction Top to Bottom. Geophysical Monograph Series Vol. 96. American Geophysical Union, Washington, D.C, pp. 11–38.
Stolper, E.D., Newman, S., 1994. The role of water in the petrogenesis of Mariana Trough Magmas. Earth Planet. Sci. Lett. 121, 293–325.
Sun, S.S., McDonough, W.F., 1989. Chemical and isotopic systematics of oceanic basalts: implication for mantle composition and processes. In: Saunders, A.D., Norry, M.J. (Eds.), Magmatism in the Oceanic Basins. Geological Society of London, pp. 313–345.
Taylor, B., 1987. A geophysical survey of the Woodlark-Solomon region. In: Taylor, B., Exon, N. (Eds.), Marine Geology, Geophysics and Geochemistry of the Woodlark Basin - Solomon Islands. Circum-Pacific Council for Energy and Mineral Resources, Houston, pp. 25–48.
Taylor, B., Exon, N.F., 1987. An investigation of ridge subduction in the Woodlark-Solomon region: introduction and overview. In: Taylor, B., Exon, N. (Eds.), Marine Geology, Geophysics and Geochemistry of the Woodlark Basin - Solomon Islands. Circum-Pacific Council for Energy and Mineral Resources, Houston, pp. 1–24.
Thirlwall, M.F., 2000. Inter-laboratory and other errors in Pb isotope analyses investigated using a ^{207}Pb-^{204}Pb double spike. Chem. Geol. 163, 299–322.
Thirlwall, M.F., 2002. Multicollector ICP-MS analysis of Pb isotopes using a ^{207}Pb-^{204}Pb double spike demonstrates up to 400 ppm/amu systematic errors in Tl-normalization. Chem. Geol. 184, 255–279.
Workman, R.k., Hart, S.R., 2005. Major and trace composition of the depleted MORB mantle (DMM). Earth Planet. Sci. Lett. 231, 53–72.
Worthing, M.A., Crawford, A.J., 1996. The igneous geochemistry and tectonic setting of metabasites from the Emo Metamorphics, Papua New Guinea; A record of the evolution and destruction of a backarc basin. Mineral. Petrol. 58, 79–100.